








RESEARCH ARTICLE | APRIL 25 2023

## Angular distribution of titanium ions and neutrals in high-power impulse magnetron sputtering discharges <sup>EP</sup>

M. Renner  ; J. Fischer   ; H. Hajihoseini  ; J. T. Gudmundsson  ; M. Rudolph  ; D. Lundin 



*J. Vac. Sci. Technol. A* 41, 033009 (2023)

<https://doi.org/10.1116/6.0002555>



# Angular distribution of titanium ions and neutrals in high-power impulse magnetron sputtering discharges

Cite as: J. Vac. Sci. Technol. A 41, 033009 (2023); doi: 10.1116/6.0002555

Submitted: 6 February 2023 · Accepted: 28 March 2023 ·

Published Online: 25 April 2023



M. Renner,<sup>1,2</sup>  J. Fischer,<sup>1,3,a)</sup>  H. Hajihoseini,<sup>4</sup>  J. T. Gudmundsson,<sup>5,6</sup>  M. Rudolph,<sup>7</sup>  and D. Lundin<sup>1</sup> 

## AFFILIATIONS

<sup>1</sup>Plasma and Coatings Physics Division, Department of Physics, Chemistry, and Biology (IFM), Linköping University, Linköping SE-58183, Sweden

<sup>2</sup>RWTH Aachen University, Aachen DE-52062, Germany

<sup>3</sup>Evatec AG, Hauptstrasse 1a, Trübbach CH-9477, Switzerland

<sup>4</sup>Industrial Focus Group XUV Optics, MESA+ Institute for Nanotechnology, University of Twente, Enschede NL-7522, The Netherlands

<sup>5</sup>Division of Space and Plasma Physics, School of Electrical Engineering and Computer Science, KTH Royal Institute of Technology, Stockholm SE-10044, Sweden

<sup>6</sup>Science Institute, University of Iceland, Reykjavik IS-107, Iceland

<sup>7</sup>Leibniz Institute of Surface Engineering (IOM), Leipzig DE-04318, Germany

<sup>a)</sup>Author to whom correspondence should be addressed: joel.fischer@liu.se

## ABSTRACT

The angular dependence of the deposition rates due to ions and neutrals in high-power impulse magnetron sputtering (HiPIMS) discharges with a titanium target were determined experimentally using a magnetically shielded and charge-selective quartz crystal microbalance (or ionmeter). These rates have been established as a function of the argon working gas pressure, the peak discharge current density, and the pulse length. For all explored cases, the total deposition rate exhibits a heart-shaped profile and the ionized flux fraction peaks on the discharge axis normal to the cathode target surface. This heart-shaped pattern is found to be amplified at increasing current densities and reduced at increased working gas pressures. Furthermore, it is confirmed that a low working gas pressure is beneficial for achieving high deposition rates and high ionized flux fractions in HiPIMS operation.

© 2023 Author(s). All article content, except where otherwise noted, is licensed under a Creative Commons Attribution (CC BY) license (<http://creativecommons.org/licenses/by/4.0/>). <https://doi.org/10.1116/6.0002555>

## I. INTRODUCTION

Physical vapor deposition (PVD) is a class of techniques used to deposit thin films and coatings in a vacuum system involving a phase transition of the film-forming material from a solid phase to a vapor or a plasma state.<sup>1</sup> PVD techniques cover a variety of methods, one of the most versatile and most widely applied being magnetron sputtering.<sup>1,2</sup> In magnetron sputtering, the atoms are released from a solid target by ion bombardment, a process referred to as sputtering. The sputtered target atoms enter the discharge volume as neutrals and often with considerable energy<sup>3,4</sup> and exhibit an angular distribution (emission profile), which depends

on target properties such as composition, history, and surface conditions, as well as energy and type of incident ions.<sup>5–8</sup> Knowledge and control of the angular distribution of the sputtered material is crucial, since it determines coating uniformity, and is therefore important for optimizing deposition processes.

The angular distribution of the sputtered flux has been reported for a number of different metal targets in dc or pulsed dc magnetron sputtering (dcMS) discharges.<sup>9–13</sup> For example, for Ti atoms sputtered from a circular titanium target in a dc magnetron sputtering (dcMS) discharge, the angular distribution is observed to be heart-shaped with a maximum located at an angle of about

40°.<sup>11</sup> Furthermore, Rogov *et al.*<sup>13</sup> explored a range of target materials and point out that the magnitude of the magnetic field and the degree of magnetic balance all have a rather small influence on the angular distribution of the neutral flux.

In dcMS discharges, the target metal flux mainly consists of neutral atoms, and, in the absence of an actual measurement, the distribution of the film-forming flux can be computed quite accurately by using a line-of-sight approach provided the erosion and emission profiles are known.<sup>14</sup> The latter can be obtained experimentally or by using one of several established analytical or numerical models.<sup>15–19</sup> The situation becomes more challenging, however, when looking at ionized PVD techniques, such as high-power impulse magnetron sputtering (HiPIMS),<sup>20–23</sup> where a significant fraction of the sputtered atoms becomes ionized. Such an increase in ionization is generally desired, as it has been shown to lead to denser films with improved adhesion<sup>24–26</sup> as well as improved film coverage of complex substrates, since the ion energy and direction can be tailored, e.g., using substrate biasing.<sup>27–29</sup> The fraction of ions in the flux of film-forming species traveling to the substrate is known as the ionized flux fraction.<sup>30</sup> Experimentally determined ionized flux fractions are typically in the range of 10%–60% and depend among other things on the target material, working gas pressure, and discharge current density.<sup>31–34</sup> While these experimental efforts have considerably improved the understanding of HiPIMS discharges, few of them offered angularly resolved information. Also, numerical predictions are much more difficult, since a second film-forming population is added and effects such as ionization and back-attraction, or more generally, interactions of the ions with the electric and magnetic fields, have to be taken into account.<sup>35</sup> Thus, up to this point, the angular distributions of the total, neutral, and ion fluxes in HiPIMS remain largely unknown.

Hajihoseini *et al.* reported on measurements of the ionized flux fraction and deposition rate in a HiPIMS discharge with a Ti target along the discharge axis<sup>33</sup> as well as perpendicular to the target surface for different magnet configurations of the magnetron assembly.<sup>36</sup> Franz *et al.* have performed angularly resolved measurements of ion fluxes by means of an energy-resolved mass spectrometer when using reactive HiPIMS to sputter niobium in an argon–oxygen atmosphere. The measurements were performed tangentially to the racetrack, and no data allowing for a direct comparison with the neutral fluxes were collected.<sup>37</sup> There have also been a few measurements of the spatiotemporal density distribution of titanium neutrals and ions in HiPIMS discharges.<sup>38–42</sup> Both Britun *et al.*<sup>38</sup> and Pajdarová *et al.*<sup>42</sup> provide laser-based density measurements of the titanium neutral and ion densities and showed that their spatial and temporal distribution in the target vicinity varies greatly. It has also been observed that a maximum in the ion density corresponds to a depletion in the neutral atom density.<sup>38,40</sup> However, as pointed out by Butler *et al.*,<sup>30</sup> it is generally not possible to directly obtain the ionized flux fraction from the densities of ions and neutrals. Therefore, the angular dependence of the ionized flux fraction and the ion deposition rate still remain largely unknown, although this information is desired to optimize the substrate position to enhance film properties as well as to improve the description of ion and neutral transport when modeling HiPIMS discharges.<sup>30</sup>

In this work, we report on the measured angular distribution of the deposition rate due to ions and neutrals and the ionized flux fraction in a HiPIMS discharge operated with Ti target. The influence of working gas pressure and peak discharge current is investigated at two different distances to the target surface and for two different pulse lengths. The paper is organized as follows: the measurement setup and experimental design are described in [Sec. II](#). The experimental results are presented and discussed in [Secs. III](#) and [IV](#), respectively. The main findings are summarized in [Sec. V](#).

## II. METHODOLOGY

### A. Experimental apparatus

The experiments were conducted in a cylindrical stainless steel deposition chamber of 42.6 cm diameter using a standard AJA ST20 unbalanced magnetron assembly and a circular Ti target of 5.08 cm diameter, 3 mm thickness, and 99.99% purity. A map of the magnetic field is provided in [Appendix C](#). The HiPIMS pulses were supplied by a HiPSTER 1 pulser unit (Ionautics AB, Sweden) which, in turn, was fed by an MDX 1K Magnetron Drive DC power supply (Advanced Energy, USA).

Argon of 99.9997% purity was used as a working gas. The argon gas flow was kept constant at 15 sccm and the working gas pressure was adjusted before igniting the discharge by partially closing a gate valve in front of the turbomolecular pump. The base pressure was kept at or below  $2 \times 10^{-4}$  Pa.

The discharge waveforms were recorded using a PicoScope 4444 20 MHz digital oscilloscope directly connected to the respective probe outputs of the HiPSTER 1 pulser unit. The average discharge power was calculated by averaging the instantaneous power over 1 s using the waveforms recorded by the PicoScope,

$$\langle P_D \rangle = \frac{1}{t} \int_0^t V_D(t') I_D(t') dt', \quad (1)$$

where  $V_D(t)$  is the discharge voltage and  $I_D(t)$  is the discharge current.

### B. Ionized flux fraction measurements

The total and neutral deposition rates were measured using a gridless QCM sensor (ionmeter), which consists of a magnetic shielding, a grounded casing, and a QCM sensor, which can be biased to achieve charge selectivity. The QCM sensor is built into the grounded casing, leaving an opening for the deposition measurements at the quartz crystal (see also [Fig. 1](#) or the sketch in Kubart *et al.*<sup>31</sup>). When measuring neutral deposition rates, the whole QCM head can be biased positively to repel the ions. Since the QCM head is built into the grounded casing, the influence of the biasing on the discharge is negligible. The magnetic shielding over the opening hole is produced by permanent magnets held in place by a magnetic yoke, whose magnetic field does not significantly affect the discharge. The operation and design of the ionmeter are described in more detail by Kubart *et al.*<sup>31</sup>

The bias was applied to the ionmeter by an Oltronix C40-08D DC power supply over a 500  $\Omega$  resistor and the voltage was fixed at 40 V. The actual bias voltage and the current drawn by the QCM

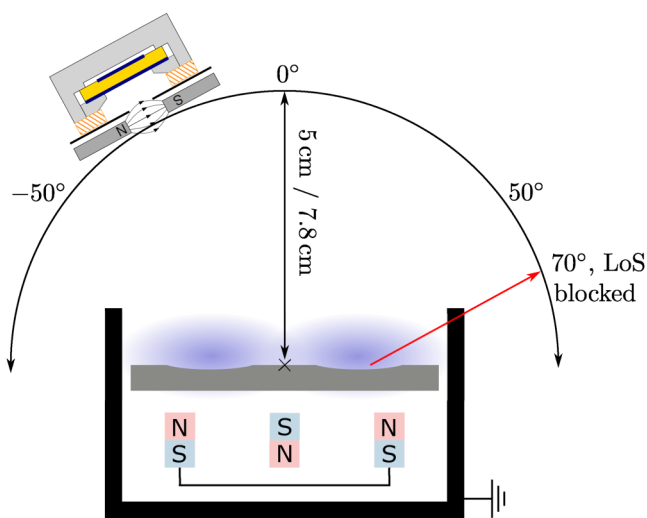


FIG. 1. Sketch of the experimental setup and the ionometer rotation. Also shown is the limited line of sight (LoS) for the largest (outermost) angles.

were recorded using a Tektronix P2220 voltage probe and a Chauvin Arnoux C160 current clamp, both connected to the same PicoScope 4444.

The QCM measurements were used to obtain deposition rates of the film-forming ions and neutrals, which, in turn, can be used to determine the ionized flux fraction  $F_{\text{flux}}$  according to Butler *et al.*,<sup>30</sup>

$$F_{\text{flux}} = \frac{R_t - R_n}{R_t}, \quad (2)$$

where  $R_t$  and  $R_n$  are the total deposition rate (sum of neutrals and ions) and the neutral deposition rate, respectively. To enhance measurement robustness and repeatability, long measurement times of 4–5 min per deposition rate measurement were chosen depending on the discharge conditions.

### C. Experimental design

For each discharge, the total and neutral deposition rates have been measured at different locations using the ionometer. The ionometer was rotated around the target, the center point of the rotation being the center of the target surface, as shown in Fig. 1. The distance from the ionometer to the target center was, therefore, fixed for each discharge. Two different distances were investigated in the present study, representing typical target to substrate distances in this deposition system. In the first case, the distance was approximately 5 cm from the top of the (grounded) magnet holder and about 5.8 cm to the quartz crystal. In the second case, the distance was increased to 7.8 cm (8.6 cm to the crystal). The 0° point is defined to be axially above the target center, and the ionometer was

rotated in steps of 10°. In the case of 5 cm target distance, 11 different angles were measured. Once the distance was increased to 7.8 cm, it was possible to rotate the ionometer further to the side and measure at 15 angles in total. Therefore, the angles at which measurements were performed spanned the range from –50° up to 50° (5 cm) and from –70° up to 70° (7.8 cm). As the setup has a symmetry axis at 0°, opposite angles are expected to give similar results.

The main operating parameters that were varied in this investigation are the peak discharge current and the working gas pressure. Additionally, the pulse length and the distance from the ionometer to the target center were varied. The peak discharge currents investigated were 10, 17, and 24 A, corresponding to peak discharge current densities of approximately 0.5, 0.8, and 1.2 A/cm<sup>2</sup>, respectively. The working gas pressure was varied between 0.3, 0.5, and 1.0 Pa. The pulse length was fixed at 100 μs for most measurements, but some additional measurements were recorded using a 50 μs pulse width. For all measurements, the average discharge power  $\langle P_D \rangle$  was kept constant at 100 W. The average power was adjusted by tuning the pulse repetition frequency until the power, as defined by Eq. (1), reached the desired value.

The experiments were divided into three measurement blocks, between which the vacuum chamber was vented to adjust the setup. In measurement block I, the full range of peak discharge currents and working gas pressures was measured while the pulse length and distance were fixed at 100 μs and 5 cm, respectively. After the first measurement block was finished, it was found that the ionometer top plate had shifted, which deteriorated the quality of the last measurement. Therefore, the chamber was vented and the ionometer assembly fixed. Afterward, in measurement block II, a repeated measurement was carried out to replace the corresponding measurement in block I. Additionally, three measurements at 50 μs pulse width were taken, varying only the working gas pressure and keeping the peak discharge current constant at 17 A. For measurement block III, the distance between target surface and ionometer was increased to 7.8 cm and the pulse width was set to 100 μs. Only the working gas pressure and peak discharge current were varied, albeit leaving out the lowest discharge current level of 10 A.

Due to the large number of cases investigated over the course of the entire study, the target was significantly eroded, amounting to a total erosion depth of about 2.1 mm. To minimize effects due to target erosion<sup>34</sup> or target and crystal heating, the discharges were measured in a randomized order within each block. An overview of the different parameters and their randomization is given in Table I. The order of the measured angles was again randomized individually for each set of parameters. The ionometer bias was varied sequentially, always first acquiring the total rate (0 V) followed by the neutral rate (40 V). During the measurement of one parameter set, the discharge was never extinguished. Additionally, vacuum was never broken between measurements belonging to the same block.

### D. dcMS reference measurements

In experiment blocks II and III, reference measurements of dcMS discharges operated at 100 W have been taken in order to normalize the deposition rate to a reference. The reference measurements were recorded for all angles at a working gas pressure of

22 May 2024 13:21:17

**TABLE I.** Order of the investigated parameter combinations. Measurement 9 was redone and is not reported.

#expr.	block	$d_{\text{target}}$ [cm]	$t_{\text{pulse}}$ [ $\mu\text{s}$ ]	$p_g$ [Pa]	$I_D$ , peak [A]	$J_D$ , peak [A/cm <sup>2</sup> ]	$f_{\text{rep}}$ [Hz]	$V_D$ [V]
11	II	5	50	0.3	17	0.84	390	480
10	II	5	50	0.5	17	0.84	364	449
13	II	5	50	1.0	17	0.84	480	374
4	I	5	100	0.3	10	0.49	265	447
3	I	5	100	0.3	17	0.84	170	474
12	II	5	100	0.3	24	1.18	125	494
8	I	5	100	0.5	10	0.49	313	429
1	I	5	100	0.5	17	0.84	170	453
2	I	5	100	0.5	24	1.18	135	461
7	I	5	100	1.0	10	0.49	480	356
5	I	5	100	1.0	17	0.84	290	381
6	I	5	100	1.0	24	1.18	198	393
18	III	7.8	100	0.3	17	0.84	170	477
19	III	7.8	100	0.3	24	1.18	130	488
17	III	7.8	100	0.5	17	0.84	195	446
14	III	7.8	100	0.5	24	1.18	137	459
16	III	7.8	100	1.0	17	0.84	285	376
15	III	7.8	100	1.0	24	1.18	198	387

0.3 Pa with a measurement time of two minutes per measurement. The normalized deposition rate was calculated using

$$R_{\text{norm}} = \frac{R_{\text{HiPIMS}}}{R_{\text{dcMS},0.3\text{Pa},0^\circ}}, \quad (3)$$

where  $R_{\text{norm}}$  is the normalized deposition rate,  $R_{\text{HiPIMS}}$  is the HiPIMS deposition rate, and  $R_{\text{dcMS},0.3\text{Pa},0^\circ}$  is the dcMS deposition rate from the reference measurement.  $R_{\text{dcMS},0.3\text{Pa},0^\circ}$  is obtained using the dcMS rates recorded at 0.3 Pa and  $0^\circ$  (along the central axis normal to the target surface) of the respective measurement block. All measurements within the same block are, therefore, normalized by the same dcMS rate. Hence, for the HiPIMS measurements recorded at 0.3 Pa and  $0^\circ$ ,  $R_{\text{norm}}$  is the same as the deposition rate fraction, which is commonly reported in the HiPIMS literature.<sup>24,43</sup>

In measurement block I, no dcMS reference measurements were taken before the ionmeter assembly changed. Therefore, in order to obtain normalized deposition rates for the first block while accounting for possible unintended changes to the ionmeter setup, additional HiPIMS measurements with the parameters from the first experiment were recorded at three angles. The block I reference rates were then approximated as the product of the dcMS rates measured in block II and the average of the ratios between the three repeated and original HiPIMS measurements.

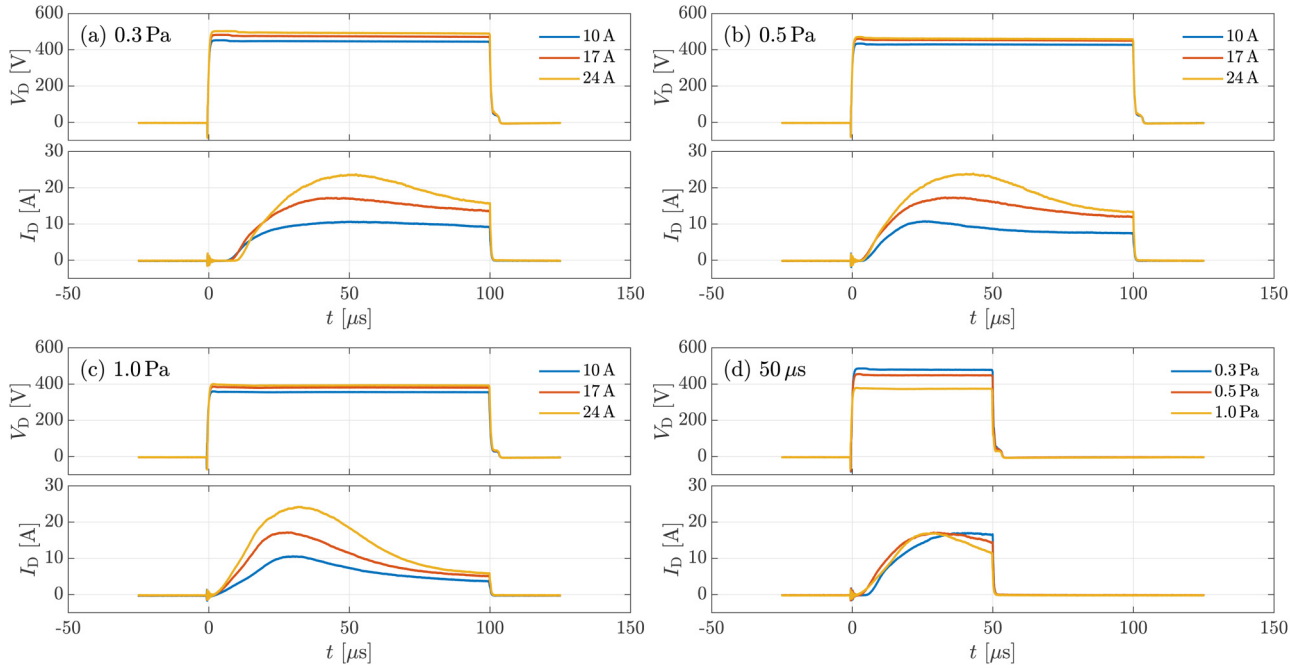


**FIG. 2.** Discharge current  $I_D$  and voltage  $V_D$  waveforms when the ionmeter is located at  $-50^\circ$  and 5 cm distance. The first three subplots show the waveforms of the HiPIMS discharges with a  $100\ \mu\text{s}$  pulse width grouped by working gas pressure: (a) 0.3, (b) 0.5, and (c) 1.0 Pa. The last subplot (d) shows the waveforms for the discharges operated with a  $50\ \mu\text{s}$  pulse width at various working gas pressures.

22 May 2024 13:21:17

### III. RESULTS

#### A. Discharge voltage and current waveforms

The waveforms of the discharge voltage and current are displayed in Fig. 2 for all the investigated discharge configurations. Figure 2(a) through (c) are grouped by working gas pressure (100  $\mu$ s pulses), whereas Fig. 2(d) shows the investigated 50  $\mu$ s long discharge pulses. The reported waveforms were measured with the ionmeter located at 5 cm from the target center in the  $-50^\circ$  position, since the interaction between ionmeter and discharge was found to be the weakest at the outermost points.

The discharge voltages are in the range of  $-356$  to  $-494$  V, as is also summarized in Table I for each pulse. The voltage pulses are very stable and hardly vary over the pulse duration. Higher peak discharge currents require higher cathode voltages, while an increase in working gas pressure significantly decreases the discharge voltage needed to achieve the desired peak discharge current. Furthermore, at high working gas pressure, the discharge current decreases faster after the peak and, hence, is lower toward the end of the pulse. For lower working gas pressures, the reduction is less significant. For more details on the discharge current evolution at different HiPIMS discharge conditions, the interested reader is referred to the work of Anders *et al.*,<sup>44</sup> which reported the discharge current waveforms for various target materials, and Lundin *et al.*,<sup>45</sup> which explored among other things the influence of the working gas pressure on the discharge current waveform. Last, it is seen that the pulses operated with a pulse length of 50  $\mu$ s [Fig. 2(d)] are not fundamentally different, except that the pulse is cut off earlier.

#### B. Peak discharge current dependencies

The recorded deposition rates for ions and neutrals for all the discharge conditions investigated can be found in Figs. 13 and 14 in Appendix A. To facilitate comparison with earlier works on HiPIMS discharges and also between different cases, we here report the total normalized deposition rate  $R_{\text{norm}}$  [defined in Eq. (3)] as well as the ionized flux fraction  $F_{\text{flux}}$  [defined in Eq. (2)]. Let us start by looking at the angular distributions of neutrals and ions for the discharges operated with 100  $\mu$ s long pulses measured at 5 cm, for which  $R_{\text{norm}}$  and  $F_{\text{flux}}$  are plotted in Figs. 3 and 4, respectively. We will investigate the angular dependence of these two quantities and the influence of the peak discharge current. Several observations can be made:

- (i) The range of ionized flux fractions measured in this work is in qualitative agreement with other measurements reported before. For example, Lundin *et al.*<sup>32</sup> measured ionized flux fractions at  $0^\circ$  in the range 31%–49% when varying the peak discharge current density  $J_{\text{D,peak}}$  in the range 0.7–1.0 A/cm<sup>2</sup> (corresponding to  $I_{\text{D,peak}} = 14$ –20 A in their and in the present setup) in a HiPIMS discharge with titanium target at 0.5 Pa Ar working gas pressure and a pulse length of 100  $\mu$ s. At a working gas pressure of 0.5 Pa, we measure ionized flux fractions in the range 14%–41%, which matches the values reported by Lundin *et al.*<sup>32</sup> fairly well. Shimizu *et al.*<sup>46</sup> report an ionized flux fraction at  $0^\circ$  in the range of about 18%–36% and a deposition rate fraction in the range from 26% down to 16% when varying the peak discharge current density

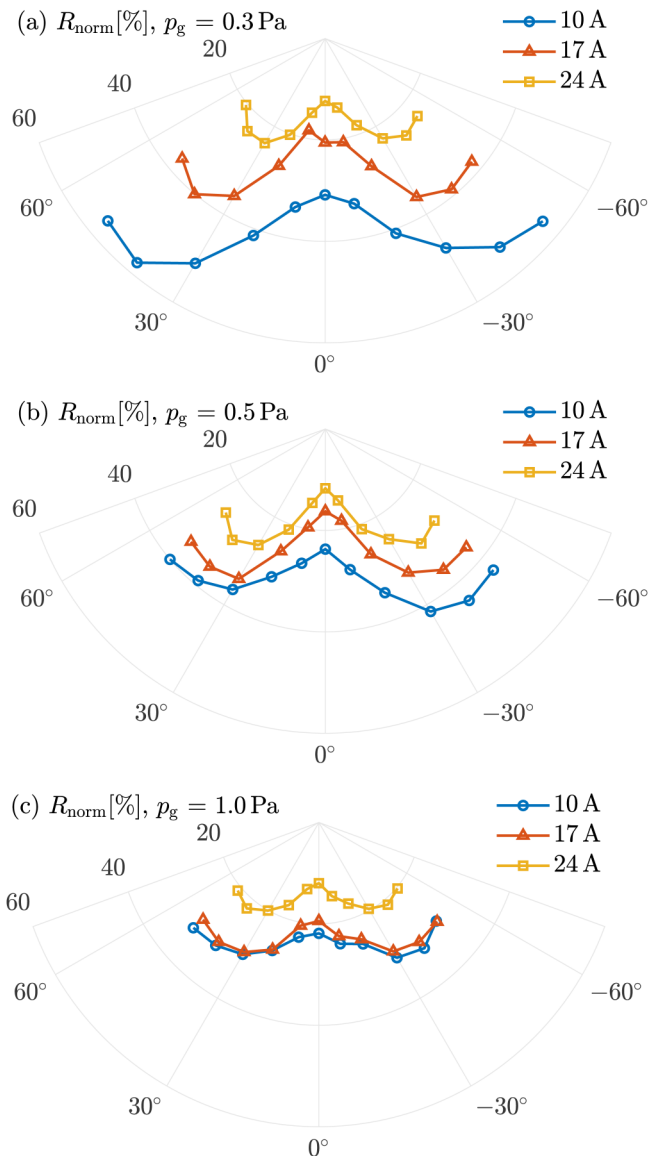
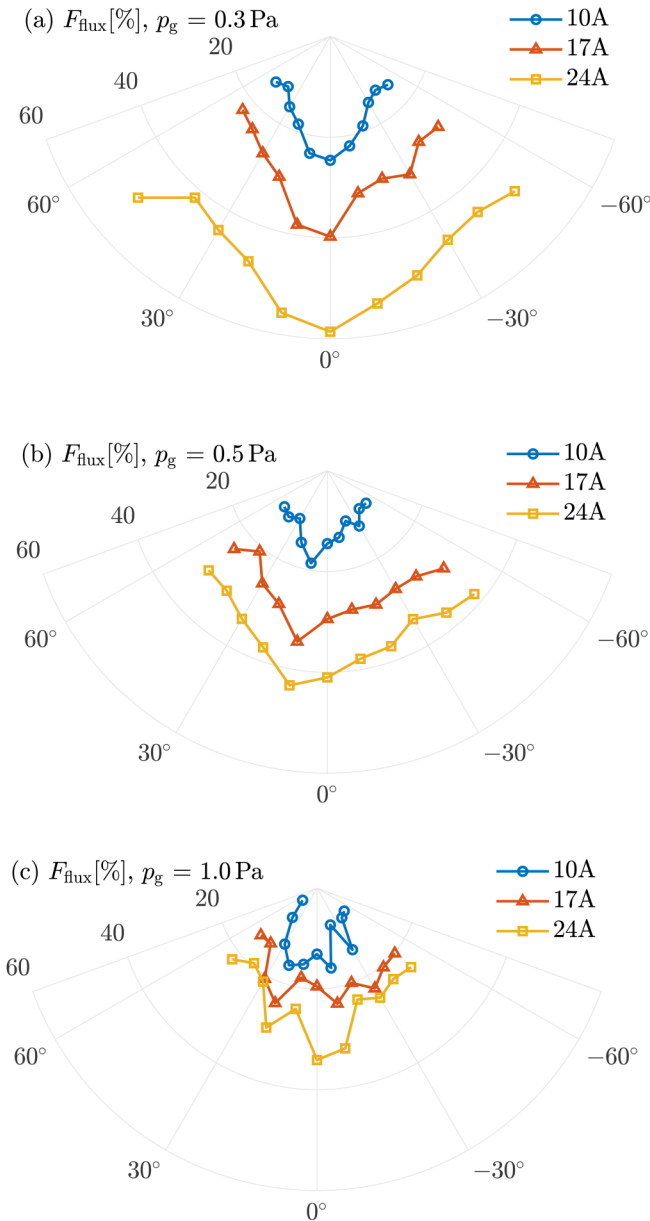


FIG. 3. Angular dependence of the normalized deposition rate for 100  $\mu$ s long pulses recorded at 5 cm distance, at (a) 0.3, (b) 0.5, and (c) 1.0 Pa working gas pressure.

$J_{\text{D,peak}}$  in the range 0.37–1.1 A/cm<sup>2</sup> (corresponding to  $I_{\text{D,peak}} = 7.5$ –22 A in the present setup) in a HiPIMS discharge with titanium target at 0.3 Pa Ar working gas pressure and a pulse length of 100  $\mu$ s. In our case, for 0.3 Pa working gas pressure, we measure ionized flux fractions in the range 25%–59% at  $0^\circ$ , and deposition rate fractions (equal to  $R_{\text{norm}}$  in this case) from 31% down to 12%, using peak discharge current densities comparable to those used by Shimizu *et al.*<sup>46</sup> (0.5–1.2 A/cm<sup>2</sup> in our study). The slight differences in the results may come from differences in the setup: both

22 May 2024 13:21:17



**FIG. 4.** Angular dependence of the ionized flux fraction for 100  $\mu$ s long pulses recorded at 5 cm distance, at (a) 0.3, (b) 0.5, and (c) 1.0 Pa working gas pressure.

works previously mentioned used different magnetron assemblies and, hence, had different magnetic field configurations. They also measured the species fluxes at a different distance from the target, and the position of the 0° point does not match exactly. Additionally, the peak discharge current densities do not match exactly, which introduces some tolerance into the comparison.

**TABLE II.** Calculated transport parameters including the reported values for the COE0 magnet configuration by Hajihoseini *et al.*

# expr.	$\xi_{ti,3cm}$	$\xi_{tn,3cm}$	$\frac{\xi_{ti,3cm}}{\xi_{tn,3cm}}$	$\xi_{ti,7cm}$	$\xi_{tn,7cm}$	$\frac{\xi_{ti,7cm}}{\xi_{tn,7cm}}$
14	0.76	0.83	0.91	0.31	0.36	0.85
15	0.75	0.79	0.95	0.31	0.33	0.95
16	0.76	0.79	0.96	0.32	0.33	0.99
17	0.76	0.83	0.91	0.32	0.35	0.91
18	0.75	0.86	0.88	0.30	0.37	0.80
19	0.75	0.87	0.87	0.29	0.39	0.76
COE0 in Ref. 58	0.61	0.76	0.8	0.16	0.3	0.52

- (ii) The ionized flux fraction increases with increased peak discharge current. Meanwhile, the deposition rate decreases with increased peak discharge current as more ions are attracted back to the cathode target. Both observations are in line with what is expected and has been reported in earlier works.<sup>35,47,48</sup>
- (iii) The deposition rate exhibits a heart-shaped pattern, with a local minimum over the center of the target and maxima between 30° and 46°. Toward the edges, the deposition rate decreases again. This heart-shaped pattern for the deposition rate has been observed and reported before for titanium sputtering in a dcMS discharge<sup>13</sup> and is further analyzed in Sec. IV C. Comparing the shapes of the normalized deposition rates of discharges operated at the same pressure but different peak current densities hints at an increasing relative importance of the lobes with increasing peak current. This is supported by the ratios between the deposition rate maxima and central minima reported in Table III. A more detailed analysis of the effect of the peak current on the shape of the ion, neutral and total fluxes is also given in Sec. IV C.
- (iv) The ionized flux fraction shows a little more scatter than the deposition rate. The increased scatter is not unexpected, since the uncertainties on the total and neutral rates are compounded when computing the ionized flux fraction. It is nevertheless clear that generally the highest ionized flux fractions are achieved at 0°, axially above the target center.

### C. Working gas pressure dependencies

Plots showing the normalized deposition rate and ionized flux fraction grouped by peak discharge current can be found in Figs. 5 and 6, respectively. We note the following general trends:

- (i) Low working gas pressures are beneficial in terms of a higher ionized flux fraction and in most cases a higher deposition rate. This observation holds for all angles and the effect is very pronounced. For example, at 0° and  $I_{D,peak} = 24$  A, the ionized flux fraction is increased from 34% to 59% while the normalized deposition rate stays constant at 12% when decreasing the pressure from 1.0 to 0.3 Pa. For 10 A at 0°,  $F_{flux}$  and  $R_{norm}$  increase from 13% to 25% and 22% to 31%, respectively, for the same reduction in working gas pressure. In most measurements, the increase of  $R_{norm}$  is even stronger

22 May 2024 13:21:17

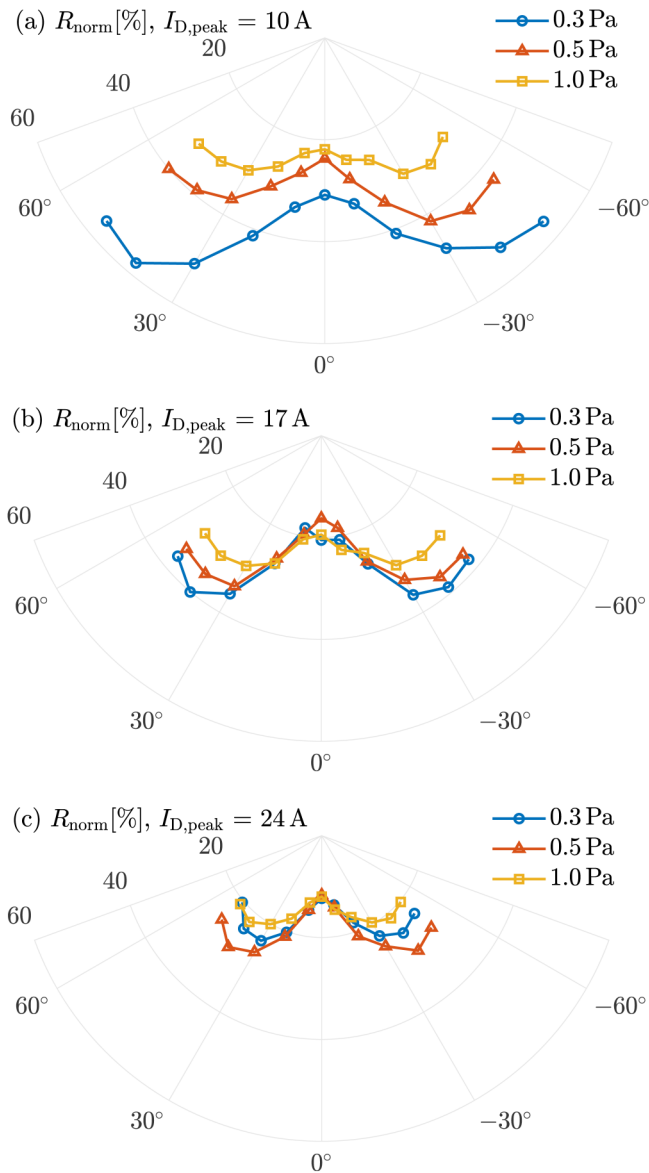


**FIG. 5.** Angular dependence of the normalized deposition rate for 100  $\mu$ s long pulses recorded at 5 cm distance, at (a) 10, (b) 17, and (c) 24 A peak discharge current.

for angles further away from the center. Indications of this dependency have been reported earlier for Ti,<sup>32</sup> where an increase of  $F_{\text{flux}}$  of about 10 percentage points was recorded for different discharge current densities when decreasing the working gas pressure from 2.0 to 0.5 Pa. However, in comparison, the present data set provides a much firmer foundation, making the observation very reliable. Furthermore, these findings confirm previous reports that suggested using as low working gas pressures as possible for optimizing the HiPIMS deposition process.<sup>35,49</sup> Only the measurements made at 0.3 Pa

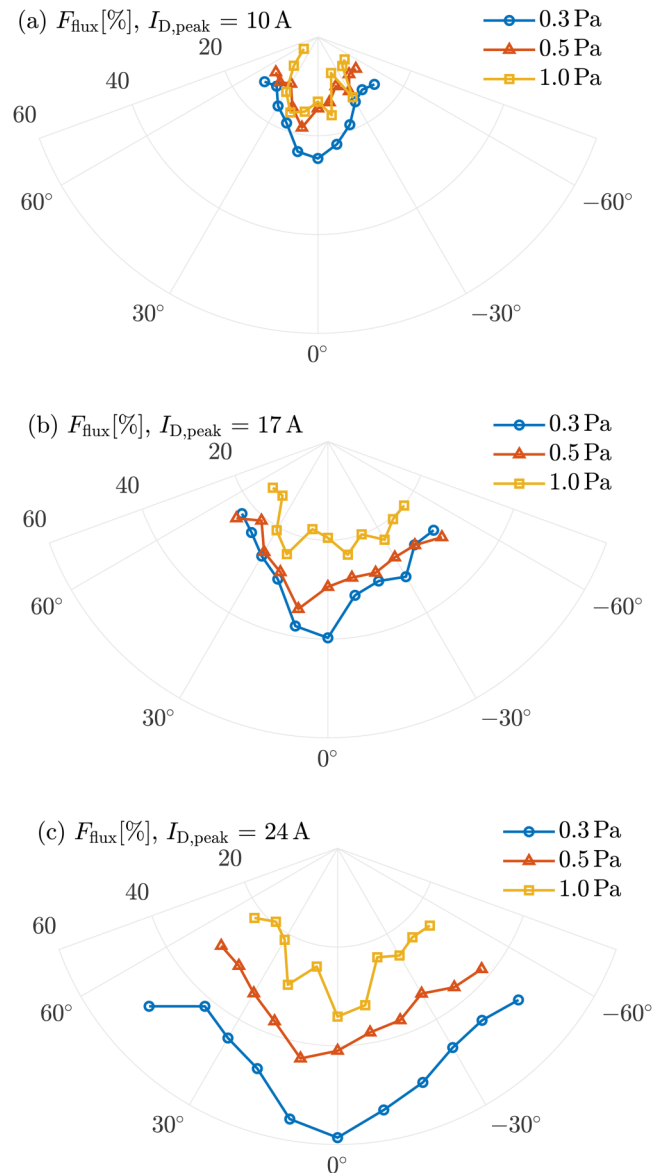


**FIG. 6.** Angular dependence of the ionized flux fraction for 100  $\mu$ s long pulses recorded at 5 cm distance, at (a) 10, (b) 17, and (c) 24 A peak discharge current.

and 24 A do not fit the deposition rate trend, but since the normalized deposition rates of different measurement blocks only allow for a qualitative comparison, this might not be a real effect and no definitive conclusion can be made.

- (ii) The deposition rate maxima are more distinct at low working gas pressures. When increasing the working gas pressure, the relative strength of the peak compared to the 0° point is reduced. For instance, at 17 A peak discharge current and 0.3 Pa working gas pressure, the normalized deposition rate is 20% at 0° and 40% at the maximum, corresponding to an

22 May 2024 13:21:17



increase of 20 percentage points. At 1.0 Pa working gas pressure and the same peak current, the normalized deposition rate increases from 19 % to 31 %, which is only 12 percentage points. This effect is a result of the reduced mean free path at high pressures, which leads to more collisions and scattering of the species and subsequently a more uniform distribution.<sup>50</sup> The mean free path for elastic Ti–Ar collisions can be estimated as follows:

$$\lambda = \frac{k_B T_g}{\sqrt{2}\pi(r_{Ar} + r_{Ti})^2 p_g}, \quad (4)$$

where  $T_g$  is the working gas temperature,  $r_{Ar}$  and  $r_{Ti}$  are the kinetic radii of Ar and Ti, respectively, and  $k_B$  is the Boltzmann constant. Using  $T_g = 500$  K,  $r_{Ar} = 169$  pm (Ref. 51) (see also Kunze *et al.*<sup>52</sup>) and  $r_{Ti} = 200$  pm,<sup>53</sup> we obtain a mean free path of 3.8 cm in the case of 0.3 Pa working gas pressure and 1.1 cm in the case of 1.0 Pa working gas pressure. Therefore, we can conclude that at low working gas pressure, still many ( $e^{-d/\lambda} = 27\%$ ) particles arrive at the point of measurement 5 cm away without being scattered, while in the case of high working gas pressure most ( $\sim 99\%$ ), particles have experienced one or more collisions before arriving at the ionmeter.

Deposition rates and ionized flux fractions for the investigated discharges with  $50 \mu\text{s}$  pulse length are shown in Fig. 7. These plots confirm the trends seen for the longer pulses that low working gas pressures enhance the deposition rate as well as the ionized flux fraction. At  $0^\circ$ , when decreasing the working gas pressure from 1.0 to 0.3 Pa, the ionized flux fraction rises nine percentage points from 34% to 43% while the deposition rate is increased by eight percentage points from 15% to 23%. As observed for the longer pulses as well, in all cases the deposition rate is heart-shaped. Furthermore, it is very clear that the highest ionized flux fraction is achieved in the center axially below the target. Comparing the results for  $t_{\text{pulse}} = 50 \mu\text{s}$  with those for  $t_{\text{pulse}} = 100 \mu\text{s}$ , it is apparent that there is always an increase in the ionized flux fraction when decreasing the pulse length while maintaining the same peak discharge current density. For instance, at  $0^\circ$ , the increase in  $F_{\text{flux}}$  is four percentage points (0.3 Pa), 13 percentage points (0.5 Pa), or 15 percentage points (1.0 Pa) while the increase at other angles is of similar magnitude. The trend between long and short pulses is less clear for the deposition rate. At 0.3 and 0.5 Pa working gas pressure, the longer pulses have a lower deposition rate near the center, but a higher deposition rate at outer angles ( $\geq 25^\circ$ ). At 1.0 Pa, the deposition rate is always lower for shorter pulses. Furthermore, the heart-shaped pattern is more pronounced in the  $100 \mu\text{s}$  long pulses. This can be seen quantitatively in Table III as well as in Fig. 11, where the sidelobes are larger (relative to the  $0^\circ$  point) for the longer pulse length.

In earlier experimental and theoretical studies,<sup>46,54</sup> the authors have seen an almost constant or, depending on peak current density, slightly decreasing or increasing ionized flux fraction, and an increase in deposition rate when reducing the pulse length down to  $50 \mu\text{s}$ <sup>46</sup> and  $40 \mu\text{s}$ <sup>54</sup> for a 152.4 mm, respectively, 101.6 mm diameter Ti target. In both cases, it was explained by a decrease in the

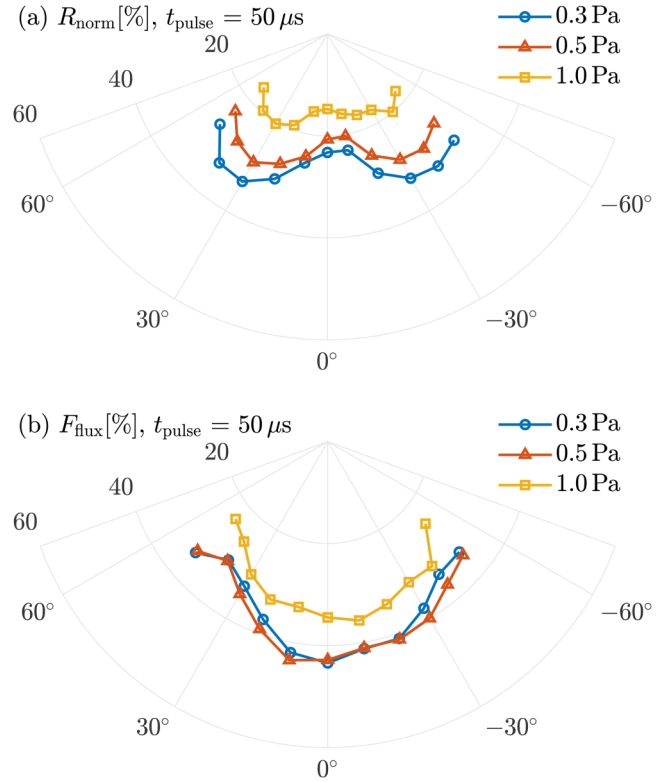


FIG. 7. Angular dependence of the (a) normalized deposition rate and (b) ionized flux fraction for the discharges with  $50 \mu\text{s}$  pulse length, which were all operated at 17 A peak discharge current (corresponding to  $0.84 \text{ A/cm}^2$ ).

average ion back-attraction probability. The reason for this was that ions present in the ionization region after the pulse are not subjected to back-attracting electric fields from the cathode anymore, while, at the same time, the relative contribution of ions (and neutrals) to the deposition rate from the afterglow increases. At the same time, a slightly decreasing metal ionization probability with shorter pulses was found when modeling those discharges,<sup>49,54</sup> although the net effect was a close-to-constant ionized flux fraction. Here, we see a strongly increasing ionized flux fraction with shorter pulses. This suggests a much stronger reduction in the average ion back-attraction with shorter pulses, while we believe that the change in metal ionization probability may be small when operating at constant peak discharge current. This would yield a higher ionized flux fraction and limited change in deposition rate with shorter pulses, which corresponds to the experimental observation. The reason for the slightly different behavior of this discharge with the earlier studies remains a matter of further investigation.

The measurement results for the six discharges which were investigated at a distance of 7.8 cm to the target are plotted in Figs. 8 and 9. At the longer distance, it was possible to extend the measurements to even larger angles (up to  $\pm 70^\circ$ ), so two more measurements at each side were taken. As also observed in the other cases, the deposition rate exhibits a heart-shaped pattern, while the

22 May 2024 13:21:17

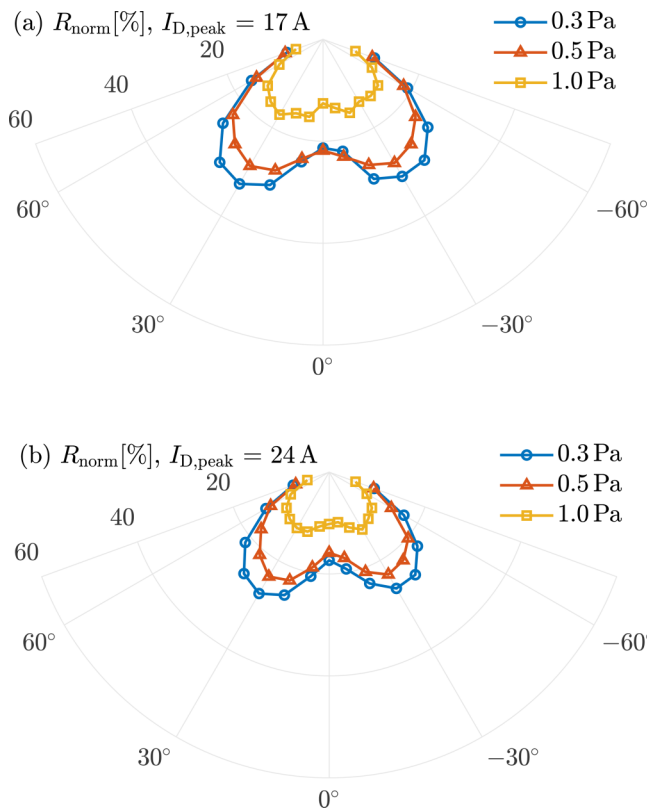


FIG. 8. Angular dependence of the normalized deposition rate for 100  $\mu$ s long pulses recorded at 7.8 cm distance, at (a) 17 and (b) 24 A peak discharge current.

ionized flux fraction peaks along the discharge axis. The results furthermore confirm the observations on the effect of low working gas pressures. In the case of 17 A peak discharge current, the ionized flux fraction at 0° increases from 22 % to 43 % and the normalized deposition rate from 13 % to 21 % when the working gas pressure is reduced from 1.0 to 0.3 Pa, which matches the measurements taken at 5 cm very well (increase from 19 % to 40 % for  $F_{\text{flux}}$  and from 19 % to 20 % for  $R_{\text{norm}}$ ). Moreover, the deposition rate is again more uniform at higher working gas pressures (in the case of 24 A: reduction from 28 % (30°) to 17 % (0°) for 0.3 Pa and from 13 % to 10 % for 1.0 Pa), again due to the reduced mean free path. Overall, the results recorded at the two different distances match sufficiently well to confirm all observations noted before.

With the additional measured angles at the sides, two more observations about the angular dependence of the deposition rate can be made. First, the deposition rate decreases continuously after peaking between 30° and 46° and falls off rapidly at  $\pm 60^\circ$  and beyond. It is furthermore seen that the ionized flux fraction increases significantly at the highest angles investigated. It is such a strong increase that at the very outermost points, ionized flux fractions of over 70 % have been measured. The reason is found in Fig. 14 in Appendix A, where the neutral deposition rate decreases much faster to the sides than the ion deposition rate.

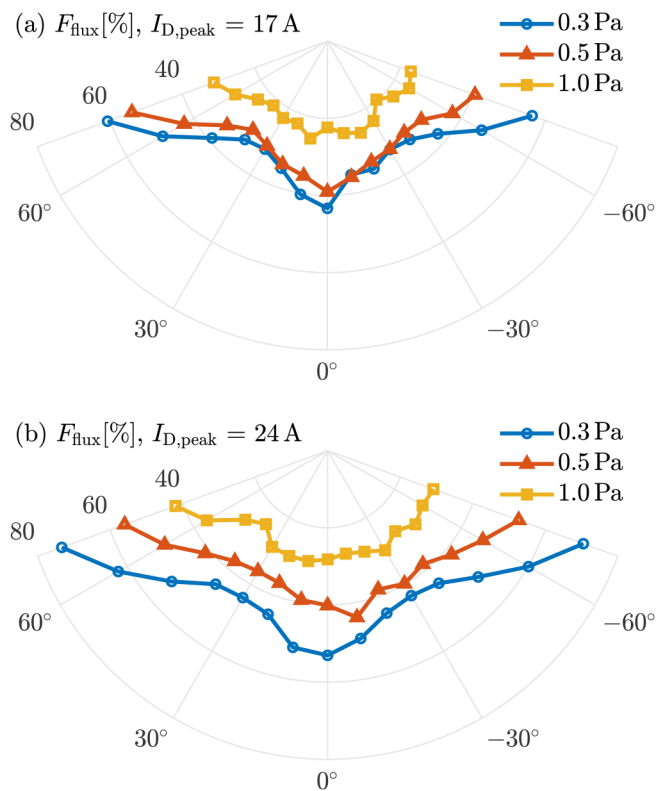


FIG. 9. Angular dependence of the ionized flux fraction for 100  $\mu$ s long pulses recorded at 7.8 cm distance, at (a) 17 and (b) 24 A peak discharge current.

22 May 2024 13:21:17

## IV. DISCUSSION

### A. Comparison to laser-based measurements

The here-reported angular dependence of the deposition rate at various process conditions all exhibit a heart-shaped profile, which typically peaks at an angle between 30° and 46° with respect to the cathode target normal, while the corresponding ionized flux fraction peaks at 0°. Comparisons of these results to the literature are difficult due to the lack of data, although we have seen in Sec. III B that values taken at 0°, axially above the target center, at different peak current densities agree well with other works. It is, furthermore, possible to make a comparison to spatially resolved laser-based density measurements of the neutral and ion densities.<sup>38–41</sup> Such comparisons are only qualitative, though, since it is generally not possible to directly obtain the ionized flux fraction from the ionized density fraction.<sup>30</sup>

Hnilica *et al.*<sup>40,41</sup> used laser-induced fluorescence in combination with atomic absorption spectroscopy to study Ti-HiPIMS discharges at different peak discharge current densities (0.6–1.7 A/cm<sup>2</sup>) and working gas pressures (0.7 and 2.7 Pa). Similar measurements have earlier been carried out by Britun *et al.*<sup>38,39</sup> Generally, the Ti atoms are seen to form two density maxima in front of the target racetrack, which then merges over the middle of the racetrack roughly 30  $\mu$ s into the pulse.<sup>40</sup> Such initial high-density regions of Ti atoms off-axis are

likely the reason for the here-observed heart-shaped profiles of Ti atoms seen in Figs. 12 and 13, since little ionization of sputtered Ti occurs during the early stage of the HiPIMS pulse due to low discharge currents.<sup>55</sup> At low working gas pressures, the Ti atoms will travel toward the substrate largely unhindered (few collisions), as discussed in Sec. III C, and thereby preserve their original distribution seen in the vicinity of the target. Furthermore, from the laser-based measurements, it is also seen that ionization of sputtered Ti increases significantly during the later stages of the discharge pulse, as the discharge current increases.<sup>40</sup> This leads to the formation of highly dense regions of Ti<sup>+</sup> ions in the close vicinity above the target racetrack,<sup>40,42</sup> although the ion density distribution becomes more homogeneous beyond a few centimeters from the target.<sup>40</sup> In our angular measurements of Ti<sup>+</sup> ions seen in Figs. 12 and 13, we do observe tendencies of heart-shaped profiles, but they are certainly not as pronounced as for the Ti neutrals, hence giving rise to the observed central peaks in  $F_{\text{flux}}$  reported in Figs. 3–9. Our measurements are carried out at typical substrate positions several centimeters away from the target and, therefore, should be subjected to a spatially more homogeneous Ti<sup>+</sup> ion flux, as indicated by the laser-based measurements.

## B. Transport parameters

For precise experimental description and computational modeling of HiPIMS discharges, geometrical factors, or transport parameters, are necessary to account for the loss of film-forming species to the chamber walls.<sup>30,56,57</sup> To that end, Christie<sup>43</sup> introduced the transport parameter  $\xi$ , that Vlček and Buralová<sup>56</sup> later split into separate transport parameters for neutral and ion species,  $\xi_{\text{tn}}$  and  $\xi_{\text{ti}}$ , respectively. The parameters relate the particle flux onto the substrate to the total sputtered particle flux. The transport parameter for each species is defined as the ratio of species arriving at the substrate over the total sputter rate (i.e., deposition rate at substrate plus chamber walls),

$$\xi_{\text{tx}} = \frac{R_{\text{tx}}^{\text{sub}}}{R_{\text{tx}}^{\text{sub}} + R_{\text{tx}}^{\text{wall}}}, \quad (5)$$

where  $\xi_{\text{tx}}$  is the transport parameter for species  $x$  (ions or neutrals),  $R_{\text{tx}}^{\text{sub}}$  is the deposition rate onto the substrate, and  $R_{\text{tx}}^{\text{wall}}$  is the deposition rate going anywhere but the substrate. Hence, the transport parameters for each type of species are defined such that  $0 \leq \xi_{\text{tx}} \leq 1$ . Recently, Hajihoseini *et al.*<sup>58</sup> used data from measurements of the deposition rate for both ions and neutrals, axially<sup>33</sup> and laterally,<sup>36</sup> to calculate transport parameters describing the ion and neutral spread in a HiPIMS discharge with Ti target. In the following, we will compare their findings to the current results by calculating the transport parameters as defined by Hajihoseini *et al.* They define a “typical” substrate of the same diameter as the target (which in their case had a diameter of 10 cm) located 3 or 7 cm axially above the target surface.

Using our measurements, it is possible to define the same virtual substrate and to calculate the same transport parameters. When transferring the definition used by Hajihoseini *et al.*<sup>58</sup> to the present setup, the typical substrate is a disk of 5 cm diameter located either 3 cm or 7 cm axially above the target surface. The typical substrate then covers all measurement angles from

$\alpha = -59^\circ$  to  $\alpha = +59^\circ$  (3 cm distance) or from  $\alpha = -36^\circ$  to  $\alpha = +36^\circ$  (7 cm distance). The deposition rate onto the typical substrate can, therefore, be calculated as

$$R^{\text{sub}} = \int_0^{2\pi} \int_0^\alpha r^2 \sin(\vartheta) F_{\text{avg}}(\vartheta) d\vartheta d\phi, \quad (6)$$

where  $F_{\text{avg}}(\vartheta)$  is the average rate of the two measurements at  $\pm\vartheta$ ,

$$F_{\text{avg}}(\vartheta) = \frac{F(\vartheta) + F(-\vartheta)}{2}. \quad (7)$$

Using the average in this way is equivalent to integrating each measurement individually over a quarter sphere. Strictly speaking,  $F$  is a rate “density” averaged over the QCM measurement area:  $F = R^{\text{QCM}}/A_{\text{QCM}}$ , but the normalization by  $A_{\text{QCM}}$  cancels out eventually.

Overall, for both ions and neutrals, the rate onto the substrate and the walls becomes

$$R^{\text{sub}} = 2\pi R^2 \int_0^\alpha \sin(\vartheta) \frac{F(\vartheta) + F(-\vartheta)}{2} d\vartheta, \quad (8)$$

$$R^{\text{wall}} = 2\pi R^2 \int_\alpha^{\pi/2} \sin(\vartheta) \frac{F(\vartheta) + F(-\vartheta)}{2} d\vartheta, \quad (9)$$

where  $R$  is the measurement distance from target surface to ion-meter. The integration was performed using the trapezoidal rule. Furthermore, the deposition rate was extrapolated to zero at  $\pm 80^\circ$ , supported by our discussion on deposition rate fits in Sec. IV C. The results are shown in Table II for the experiments 14–19 (see

**TABLE III.** Ratio of maximum deposition rate to rate at  $0^\circ$  for ions and neutrals. The peak of the neutral rate is generally more distinct than the peak of the ion rate.

$p_g$ [Pa]	$I_D$ , peak [A]	$J_D$ , peak [A/cm <sup>2</sup> ]	$t_{\text{pulse}}$ [μs]	$d_{\text{target}}$ [cm]	$\max(R_n)/R_{n,0^\circ}$ —	$\max(R_i)/R_{i,0^\circ}$ —
0.3	17	0.84	50	5	1.75	1.22
0.5	17	0.84	50	5	1.62	1.29
1.0	17	0.84	50	5	1.51	1.25
0.3	10	0.49	100	5	2.16	1.10
0.3	17	0.84	100	5	2.46	1.40
0.3	24	1.18	100	5	2.72	1.58
0.5	10	0.49	100	5	1.96	1.54
0.5	17	0.84	100	5	2.45	2.29
0.5	24	1.18	100	5	2.85	2.26
1.0	10	0.49	100	5	1.64	1.53
1.0	17	0.84	100	5	1.68	1.78
1.0	24	1.18	100	5	2.26	1.25
0.3	17	0.84	100	7.8	1.83	1.15
0.3	24	1.18	100	7.8	1.90	1.32
0.5	17	0.84	100	7.8	1.48	1.09
0.5	24	1.18	100	7.8	1.60	1.45
1.0	17	0.84	100	7.8	1.35	1.41
1.0	24	1.18	100	7.8	1.25	1.35

22 May 2024 13:21:17

Table I for experimental details). These are the experiments with additional measurement points at the sides—deposition rates are plotted in Fig. 14.

In order to make a fair comparison, we first need to identify reasonably similar experimental conditions. The experiments reported by Hajihoseini *et al.*<sup>58</sup> were taken at different conditions: 10 cm target diameter, average power  $\langle P_D \rangle = 300$  W, working gas pressure of 1.0 Pa, 100  $\mu$ s long pulse, and varying discharge current density  $J_D(t)$ . For comparison, we take the strongest magnet configuration C0E0, in which case the peak discharge current density was 1 A/cm<sup>2</sup>. Hence, the conditions in experiments 15 and 16 in this work are very close to the discharges investigated by Hajihoseini *et al.*<sup>58</sup> Despite differences in both size and design of the used magnetron assemblies, the values are generally in good agreement with those obtained by Hajihoseini *et al.* However, it can be noted that the ion transport parameter is larger in the present measurements, especially for the substrate located at a distance of 7 cm from the target.

### C. Deposition rate fit

The total deposition rate and the separate deposition rates due to neutral and ions, respectively, are well approximated by the empirical formula proposed by Martynenko *et al.*<sup>11</sup>

$$f(\theta) = A \cos^n \theta - B \cos^m \theta, \quad (10)$$

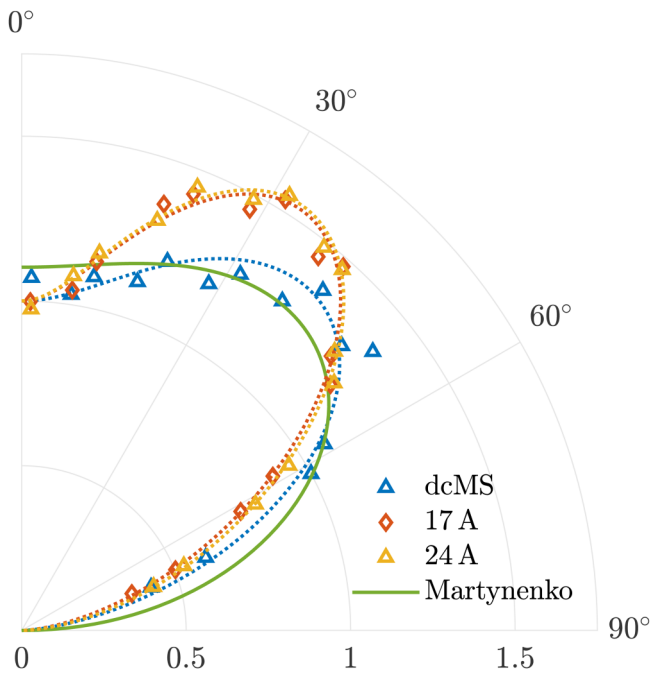


FIG. 10. Measured and fitted total deposition rates at 7.8 cm and at 0.3 Pa (dcMS and HiPIMS) compared to the approximation provided by Martynenko *et al.*<sup>11</sup> The measurement data are scaled such that the fitted deposition rates are unitary at the vertical axis. The approximation by Martynenko *et al.* is scaled to best fit the dcMS measurement.

which has been shown to accurately reproduce the angular dependence of the deposition rate in dcMS for a wide variety of target materials.<sup>11,13</sup> In addition to the fitting parameters  $A$ ,  $B$ ,  $n$ , and  $m$ , an angular shift  $\theta_0$ , such that  $\theta = \theta_{\text{measured}} - \theta_0$ , has been introduced to account for possible systematic deviations in the measurement angle that are due to the limitations of the experimental setup.

An illustrative example is shown in Fig. 10, where the angularly resolved dcMS deposition rate measured by Martynenko *et al.* is compared to the dcMS reference measurement performed as part of this study, as well as the HiPIMS measurements at the same pressure and at a distance of 7.8 cm from the target center. The dcMS reference measurement agrees reasonably well with the approximation provided by Martynenko *et al.*,<sup>11</sup> especially considering inevitable differences in the discharge conditions and measurement setup. The comparison with the total deposition rate in the corresponding HiPIMS discharges also illustrates that, while the maximum is closer to the normal, the total flux in HiPIMS features more pronounced lobes—a trend that persists in the other low pressure ( $p_g \lesssim 1.0$  Pa) HiPIMS discharges.

Last, the total deposition rates for the two HiPIMS measurements shown in Fig. 10 almost coincide. However, it should be noted that, while typically the change in the distribution of the total flux is smaller than those of the neutral or ion fluxes when going from 17 to 24 A, generally there are still significant differences.

The remaining cases are shown in Appendix B together with a complete list of fitting parameter values.

In addition to being useful for modeling purposes, these fits also enable the quantification of the changes in the shape of the angular distributions when varying the process parameters. The first row in Fig. 11 shows the relative importance of the lobes for the total, neutral, and ion distributions as measured by the ratio of the maximum and central minimum of the deposition rates  $R_{\text{max}}/R_0 = \max(f(\theta))/f(0^\circ)$ , with  $f(\theta)$  from Eq. (10). As previously noted in Sec. III B, the lobes increase in size as the peak current is increased. This is true for all three distributions, however, the effect is especially strong for the neutrals. There is a clear separation between the measurements at 7.8 cm and their counterparts at 5 cm, which might be explained by increased scattering due to the larger distance. Although there are some exceptions, the trend of decreasing relative strength of the peaks with increasing working gas pressure already noted in Sec. III C is also shown clearly. Finally, we can also note that the 50  $\mu$ s pulse length discharges have considerably less pronounced lobes compared to the corresponding 100  $\mu$ s discharges. The second row shows the angles  $\theta_{\text{max}} = \arg \max(f(\theta))$  at which the maxima of the different distributions occur. There is again a clear distinction between the corresponding measurements at 7.8 and 5 cm. In the former case, the peaks are located between 30° and 35° while for the latter the maxima are attained between 38° and 46°. The expectation value of the emission angle, calculated as

$$\mathbb{E}(\theta) = \frac{\int_0^{\pi/2} \theta f(\theta) \sin \theta d\theta}{\int_0^{\pi/2} f(\theta) \sin \theta d\theta} \quad (11)$$

is displayed in the last row. It incorporates information from the

22 May 2024 13:21:17

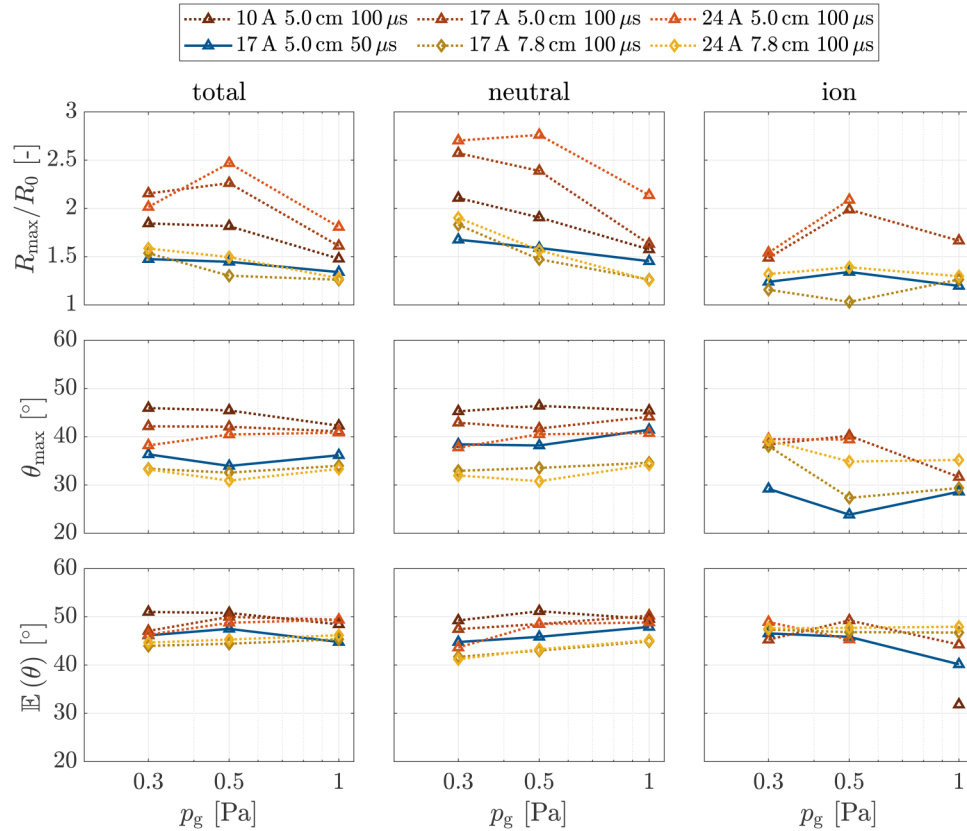


**FIG. 11.** Relative strength ( $R_{\max}/R_0$ ) and location ( $\theta_{\max}$ ) of the lobes, as well as the expected value of the emission angle  $\mathbb{E}(\theta)$  for each angular distribution (total, neutral, and ion fluxes). The cases for which the quality of the ion flux distribution fits was insufficient ( $R^2 < 0$ ) are excluded from the plots displaying properties of the ion flux distribution.

22 May 2024 13:21:17

entire distribution. As a consequence, the values for the measurements performed at 5 cm are of limited reliability, since the corresponding fits are underdetermined at shallow angles. In general, we can nevertheless note the relatively small spread. Remarkable is, however, that for the measurements performed at 7.8 cm, for which the fits are very accurate, there seems to be almost no dependence on the peak discharge current. Furthermore, in the case of the ions, there is also virtually no dependence on the pressure in the explored range.

## V. CONCLUSION

We have determined the angular dependence of the deposition rates for ions and neutrals in a high-power impulse magnetron sputtering (HiPIMS) discharge with a titanium target. The rates were determined as the argon working gas pressure, the peak discharge current density, and the pulse length were varied. For all the cases explored, the total deposition rate exhibits a heart-shaped profile, while the ionized flux fraction peaks on the central axis normal to the cathode target surface.

Furthermore, we investigated the influence of the varied process conditions on the angular distribution of both species. The heart-shaped pattern becomes more distinct for higher peak discharge currents and less distinct for increased working gas pressure. We could also confirm that a low working gas pressure is beneficial for achieving high deposition rates as well as high ionized flux fractions. We, furthermore, used the results to compute transport parameters, which are frequently used in computational modeling, and to fit the measurement curves to a suitable formula from the literature. Using both methods, we obtained good results, which can be used to further improve our understanding of HiPIMS discharges.

## ACKNOWLEDGMENTS

This work was partially funded by the Swedish Research Council (Grant No. VR 2018-04139), the Swedish Government Strategic Research Area in Materials Science on Functional Materials at Linköping University (Faculty Grant SFO-Mat-LiU No. 2009-00971), the Icelandic Research Fund (Grant No. 196141), and Evatec AG.

**AUTHOR DECLARATIONS**

**Conflict of Interest**

The authors have no conflicts to disclose.

**Author Contributions**

**M. Renner:** Formal analysis (equal); Investigation (lead); Methodology (equal); Visualization (equal); Writing – original draft (equal); Writing – review & editing (equal). **J. Fischer:** Formal analysis (equal); Investigation (supporting) Methodology (equal); Visualization (equal); Writing – review & editing (equal). **H. Hajihoseini:** Writing – review & editing (equal). **J. T. Gudmundsson:** Writing – review & editing (equal). **M. Rudolph:** Writing – review & editing (equal). **D. Lundin:** Conceptualization (equal); Funding acquisition (equal); Resources (equal); Supervision (equal); Writing – review & editing (equal).

**DATA AVAILABILITY**

The data that support the findings of this study are available from the corresponding author upon reasonable request.

**APPENDIX A: ION AND NEUTRAL DEPOSITION RATES**

The recorded normalized deposition rates for ions and neutrals for all the discharge conditions investigated are given in Figs. 12–14. In many cases, it is seen that the deposition rate of ions peaks off-axis at around 30°–40°. This is in agreement with laser-based measurements by Britun *et al.*,<sup>38</sup> which were recorded at working gas pressure 0.7 Pa. At high working gas pressures (2.7 and 10.7 Pa), they also report a third peak evolving axially from the target center (corresponding to 0° in our measurements), which is not seen here. The reason is likely that we are operating at a maximum working gas pressure of 1.0 Pa, as Britun *et al.* also did not detect a third peak when operating at 0.67 Pa.

From our measurements, it is also seen that the peaks in the ion deposition rates are generally weaker than the peaks of the neutral deposition rates relative to the minimum at 0°. Table III quantifies that observation by displaying the ratio of the maximum recorded deposition rate compared to the rate at 0°, for each discharge, both for ions and neutrals. Except for three measurements (all at 1.0 Pa), the fraction  $\max(R_n)/R_{n,0^\circ}$  is always stronger than the corresponding fraction  $\max(R_i)/R_{i,0^\circ}$ . This has a significant impact on the ionized flux fraction and is the reason for its peak at the center, which was described in

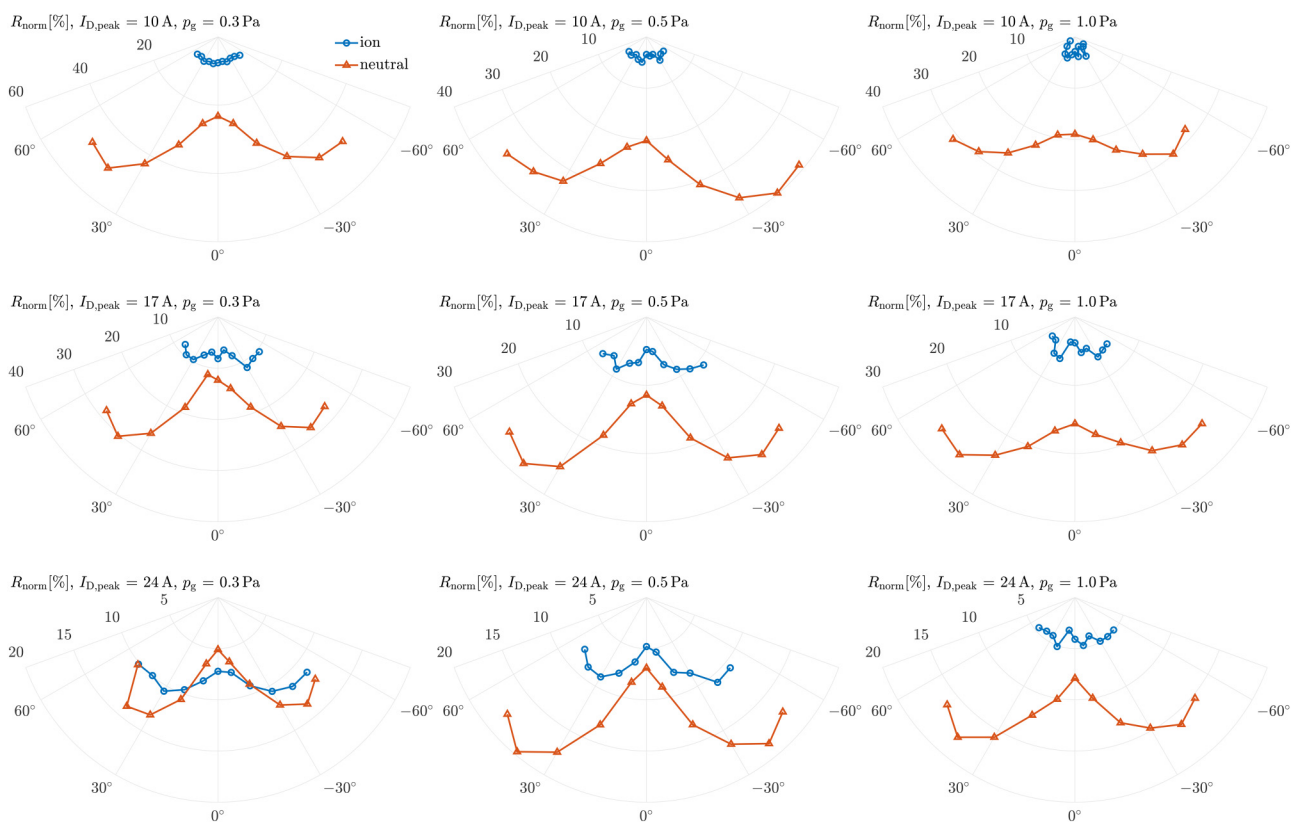


**FIG. 12.** Angular distribution of the neutrals (red triangles) and ions (blue circles) for 100 μs long pulses recorded at 5 cm distance.

22 May 2024 13:21:17

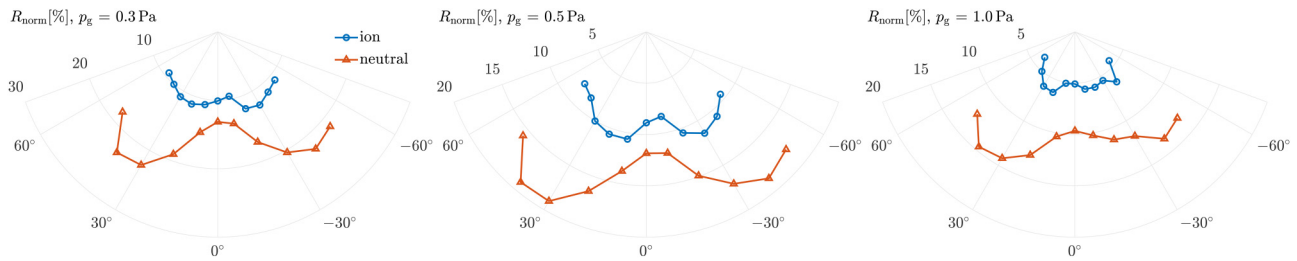


**FIG. 13.** Angular distribution of the neutrals (red triangles) and ions (blue circles) for the measurements with 50  $\mu\text{s}$  long pulses and 17 A peak discharge current.

**Sec. III.** As a side note, we believe that these results could be a guide when performing the known tradeoff of deposition rate vs ionized flux fraction (sometimes referred to as the HiPIMS compromise<sup>35</sup>) by adjusting the substrate position according to the requirements of the deposited thin film, although this is out of scope of the present work.

Finally, it is worth noting that for the data points at angles larger than  $\pm 50^\circ$  the ionmeter is already partially shadowed by the ground shield of the magnetron assembly, which is illustrated in Fig. 1. During those high-angle measurements, we find that the outer edges of the target racetrack closest to the ionmeter have no line of sight to the sensor. We, therefore, assume that the rates recorded during these conditions are a result of particles ejected from other parts of the racetrack or arrived there through collisions and scattering.

**APPENDIX B: FITTED DEPOSITION RATES**

The total, neutral, and ion deposition rate fits for the measurements performed at 5 cm from the target center and a pulse length of 100  $\mu\text{s}$  are shown in Fig. 15. The fits for the measurements at 5 cm from the target center but at shorter pulse length and the measurements at 7.8 cm are shown in Fig. 16 and Fig. 17, respectively. The found values for the fitting parameters are listed in Table IV together with the adjusted coefficient of determination  $\bar{R}^2$  to give a quantification of the goodness of the fits. It should be noted, however, that the values for the fitting parameters  $A$ ,  $B$ ,  $n$ , and  $m$  carry little meaning in themselves.

While Eq. (10) is remarkably well suited for approximating the angular dependence of the measured total and neutral rate, the quality of the ion deposition rates fits is not as good. The good fits for the measurements at 7.8 cm (c.f. experiments 14 through 19 in

22 May 2024 13:21:17

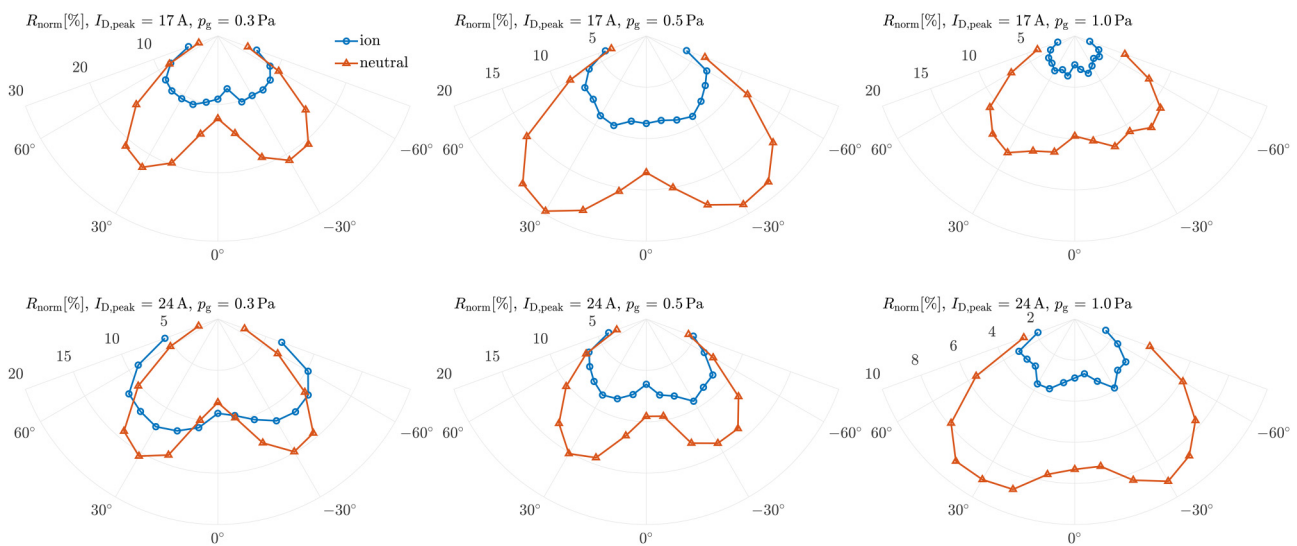


**FIG. 14.** Angular distribution of the neutrals (red triangles) and ions (blue circles) for 100  $\mu\text{s}$  long pulses recorded at 7.8 cm distance.

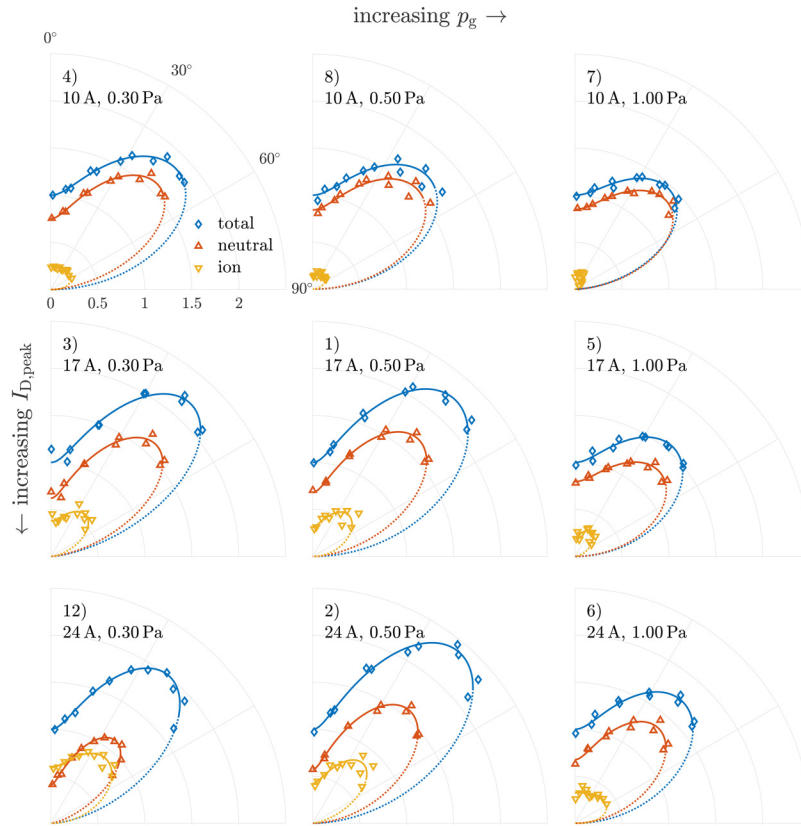


**FIG. 15.** Angle adjusted measured total, neutral, and ion deposition rates for the measurement series at 5 cm from the target center with  $100\ \mu\text{s}$  pulses, fitted according to Eq. (10). The deposition rates are normalized such that the total deposition rate at  $0^\circ$  is unitary while the relative deposition rate due to neutrals and ions is maintained. The cases are organized with increasing pressure from left to right and increasing peak current from top to bottom. The corresponding experiment numbers together with the relevant process parameters are shown in the top left corner of each figure.

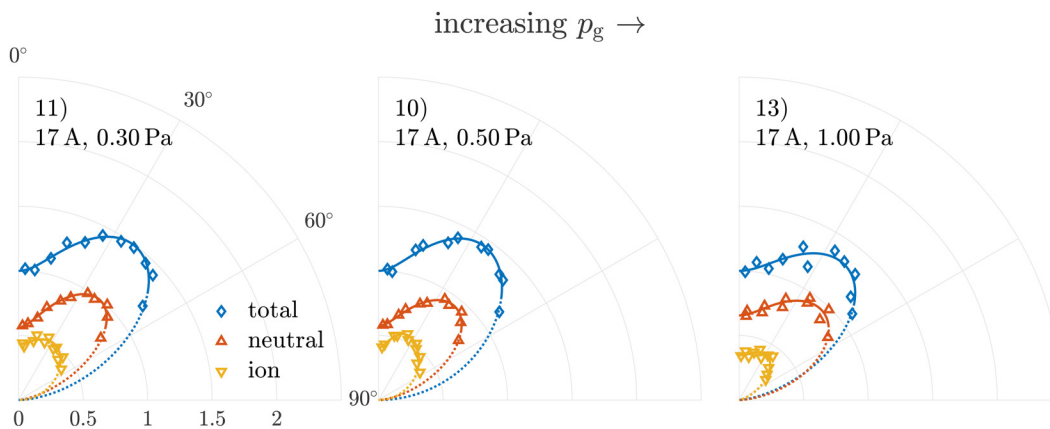


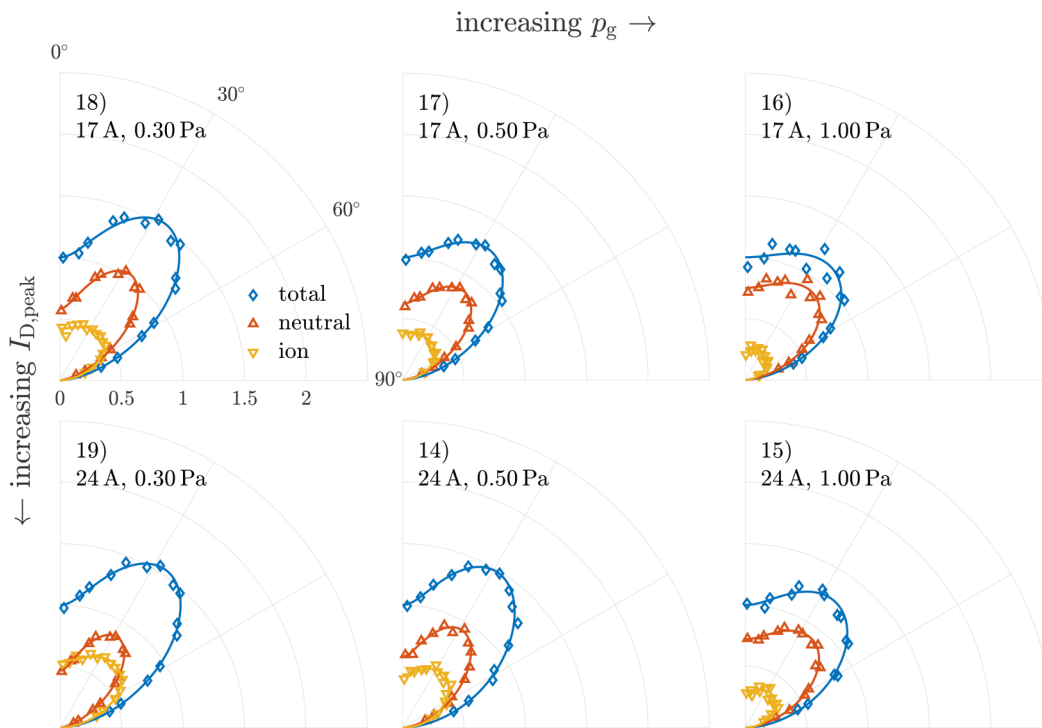
**FIG. 16.** Angle adjusted measured total, neutral, and ion deposition rates for the measurement series at 5 cm from the target center with  $50\ \mu\text{s}$  pulses, fitted according to Eq. (10). The deposition rates are normalized such that the total deposition rate at  $0^\circ$  is unitary while the relative deposition rate due to neutrals and ions is maintained. The cases are organized with increasing pressure from left to right, and the corresponding experiment numbers together with the relevant process parameters are shown in the top left corner of each figure.

22 May 2024 13:21:17



**TABLE IV.** Fitting parameter values from Eq. (10) for the total, neutral, and ion deposition rates. The values of  $\theta_0$  are below  $5^\circ$  for all total and neutral rate fits. The adjusted coefficients of determination  $\bar{R}^2$  (5 degrees of freedom) are also given.

# expr.	Total					Neutral					Ion				
	A	n	B	m	$\bar{R}^2$	A	n	B	m	$\bar{R}^2$	A	n	B	m	$\bar{R}^2$
1	2.83	0.52	1.83	8.13	0.99	4.91	1.36	3.93	5.14	0.98	2.38	0.50	1.33	9.72	0.64
2	4.05	1.17	3.05	6.30	0.98	4.73	1.26	3.76	6.29	0.99	15.9	2.56	14.8	3.39	0.78
3	20.6	2.35	19.6	2.99	0.96	21.9	2.32	20.9	3.08	0.96	15.2	2.45	14.2	3.00	0.45
4	3.78	1.04	2.78	3.64	0.99	7.54	1.57	6.55	3.07	0.99	2.12	0.50	1.13	1.31	-0.17
5	1.93	0.50	0.93	7.61	0.95	2.76	0.90	1.76	4.11	0.96	2.47	1.51	1.43	9.68	0.26
6	2.20	0.58	1.20	7.71	0.97	3.57	1.15	2.53	5.64	0.94	4.33	0.55	3.36	0.92	-0.18
7	3.74	1.34	2.74	3.23	0.95	9.17	1.61	8.20	2.30	0.97	3.19	0.50	1.90	0.00	0.27
8	2.26	0.50	1.26	5.61	0.93	2.40	0.50	1.42	5.49	0.94	1.45	0.50	0.51	27.3	0.09
10	1.79	0.78	0.79	11.2	0.97	4.01	1.75	3.03	4.48	0.98	1.44	0.75	0.46	38.7	0.90
11	2.68	1.41	1.68	5.77	0.96	13.9	2.61	12.9	3.40	0.98	1.32	0.50	0.32	41.5	0.71
12	4.06	1.59	3.06	5.77	0.98	28.0	3.19	27.0	4.00	0.98	1.82	0.50	0.82	9.18	0.86
13	5.54	2.12	4.54	3.41	0.73	5.69	1.67	4.69	2.83	0.84	7.72	3.18	6.71	4.15	0.66
14	2.03	1.26	1.03	11.0	0.99	2.40	1.67	1.43	10.1	0.99	1.73	0.82	0.68	10.1	0.92
15	1.94	1.22	0.94	6.46	0.97	2.54	1.59	1.55	4.71	0.98	1.55	0.73	0.53	13.3	0.73
16	3.56	1.77	2.56	3.24	0.92	4.85	2.01	3.88	3.12	0.94	4.53	1.53	3.41	2.24	0.73
17	2.28	1.58	1.28	5.94	0.99	3.70	2.16	2.68	5.13	0.99	3.01	1.41	2.02	2.33	0.96
18	2.76	1.72	1.76	7.09	0.99	4.52	2.48	3.49	6.58	0.99	6.66	1.71	5.68	2.31	0.90
19	2.51	1.52	1.51	7.92	0.99	4.10	2.47	3.11	7.70	1.00	3.76	1.47	2.74	2.93	0.96



22 May 2024 13:21:17

**FIG. 17.** Angle adjusted measured total, neutral, and ion deposition rates for the measurement series at 7.8 cm from the target center with  $100\ \mu\text{s}$  pulses, fitted according to Eq. (10). The deposition rates are normalized such that the total deposition rate at  $0^\circ$  is unitary while the relative deposition rate due to neutrals and ions is maintained. The cases are organized with increasing pressure from left to right and increasing peak current from top to bottom. The corresponding experiment numbers together with the relevant process parameters are shown in the top left corner of each figure.

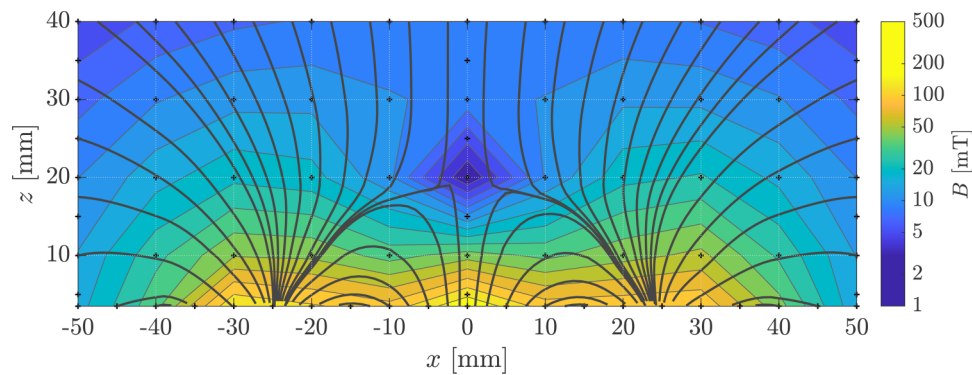


**FIG. 18.** Magnetic field as measured in a vertical plane passing through the center of one of the outer magnets and the center of the central magnet. Field lines are drawn to better illustrate the magnetic topology, however the spacing is heuristic and does not reflect the actual magnetic field strength, which is instead displayed using a logarithmic color scale. The individual measurement points used to reconstruct the magnetic field are marked with small crosses. The lowest measurement points are located at  $z = 3.5$  mm from the magnetron surface, or 0.5 mm from the target surface. The slight asymmetry in the  $x$ -direction is expected, since, due to the odd number of outer magnets, the plane passes through in between two magnets on the positive  $x$  side.

Table IV and Fig. 17) show, however, that this is not because Eq. (10) is not well suited but rather due to the noisier data in a consequence of the fact that errors on both the angle and the rate from the total and neutral deposition rate measurements are compounded in the values for the ion deposition rate.

Furthermore, while overfitting does not seem to be an issue, one should keep in mind that the number of degrees of freedom, five including the zero angle offset, is quite high. In the case of the measurements performed at 5 cm, there are no measurement points beyond  $60^\circ$  and the fit in that region is underdetermined. Therefore, drawing any conclusions from the fitted rates at these shallow angles, in particular, with respect to the breadth of the lobes, should be avoided.

### APPENDIX C: MAGNETIC FIELD TOPOLOGY

While the effect of the magnetic field topology on the angular dependence of the ion and neutral fluxes is not investigated in the presented work, its influence can be expected to be significant, thus warranting the inclusion of a more detailed description. The AJA ST20 magnetron assembly used in this study features a cylindrical center magnet ( $\approx 485$  mT) and 13 cylindrical outer magnets ( $\approx -370$  mT) arranged on a circle at  $r = 25.4$  mm from the magnetron assembly center. A map of the magnetic field, acquired using a LakeShore MMT-6J04-VH Hall sensor, is shown in Fig. 18. The magnetic null point is located at  $z_{\text{null}} = 18$  mm from the magnetron assembly surface respectively at 15 mm from the target surface. At 0.5 mm from the target surface, the highest axial magnetic field is  $B_{z,\text{max}} = 205$  mT ( $r = 0$  mm) and the highest radial field is  $B_{r,\text{max}} = 112$  mT ( $r = 4.5$  mm).

### REFERENCES

<sup>1</sup>J. T. Gudmundsson, A. Anders, and A. von Keudell, *Plasma Sources Sci. Technol.* **31**, 083001 (2022).  
<sup>2</sup>J. T. Gudmundsson, *Plasma Sources Sci. Technol.* **29**, 113001 (2020).  
<sup>3</sup>M. W. Thompson, *Philos. Mag.* **18**, 377 (1968).

<sup>4</sup>M. Stepanova and S. K. Dew, *Nucl. Instrum. Methods Phys. Res. Sect. B* **215**, 357 (2004).  
<sup>5</sup>R. Behrisch and K. Wittmaack, "Introduction," in *Sputtering by Particle Bombardment III, Topics in Applied Physics*, edited by R. Behrisch and K. Wittmaack (Springer Verlag, Berlin, 1991), Vol. 64, pp. 1–13.  
<sup>6</sup>Y. Yamamura and H. Tawara, *At. Data Nucl. Data Tables* **62**, 149 (1996).  
<sup>7</sup>W. Eckstein, "Sputtering yields," in *Sputtering by Particle Bombardment: Experiments and Computer Calculations from Threshold to MeV Energies, Topics in Applied Physics*, edited by R. Behrisch and W. Eckstein (Springer Verlag, Berlin, 2007), Vol. 110, pp. 33–187.  
<sup>8</sup>R. Behrisch and W. Eckstein, "Introduction and overview," in *Sputtering by Particle Bombardment: Experiments and Computer Calculations from Threshold to MeV Energies, Topics in Applied Physics*, edited by R. Behrisch and W. Eckstein (Springer Verlag, Berlin, 2007), Vol. 110, Chap. 1, pp. 1–10.  
<sup>9</sup>G. M. Turner, S. M. Rossnagel, and J. J. Cuomo, *J. Appl. Phys.* **75**, 3611 (1994).  
<sup>10</sup>M. Horkel, K. Van Aeken, C. Eisenmenger-Sittner, D. Depla, S. Mahieu, and W. P. Leroy, *J. Phys. D: Appl. Phys.* **43**, 075302 (2010).  
<sup>11</sup>Y. V. Martynenko, A. V. Rogov, and V. I. Shul'ga, *Tech. Phys.* **57**, 439 (2012).  
<sup>12</sup>D. V. Sidelev and V. P. Krivobokov, *Vacuum* **160**, 418 (2019).  
<sup>13</sup>A. V. Rogov and Y. V. Kapustin, *Instrum. Exp. Tech.* **63**, 776 (2020).  
<sup>14</sup>A. V. Rogov and Y. V. Kapustin, *Instrum. Exp. Tech.* **62**, 109 (2019).  
<sup>15</sup>Y. Yamamura, *Radiat. Eff. Defects Solids* **55**, 49 (1981).  
<sup>16</sup>Y. Yamamura, T. Takiguchi, and M. Ishida, *Radiat. Eff. Defects Solids* **118**, 237 (1991).  
<sup>17</sup>V. Shul'ga, *Nucl. Instrum. Methods Phys. Res. B* **164–165**, 733 (2000).  
<sup>18</sup>M. Stepanova and S. K. Dew, *J. Vac. Sci. Technol. A* **19**, 2805 (2001).  
<sup>19</sup>J. F. Ziegler, J. P. Biersack, and M. D. Ziegler, *SRIM—The Stopping and Range of Ions in Matter* (SRIM Co., Chester, Maryland, 2008).  
<sup>20</sup>U. Helmersson, M. Lattemann, J. Bohlmark, A. P. Ehiasarian, and J. T. Gudmundsson, *Thin Solid Films* **513**, 1 (2006).  
<sup>21</sup>J. T. Gudmundsson, N. Brenning, D. Lundin, and U. Helmersson, *J. Vac. Sci. Technol. A* **30**, 030801 (2012).  
<sup>22</sup>D. Lundin and K. Sarakinos, *J. Mater. Res.* **27**, 780 (2012).  
<sup>23</sup>*High Power Impulse Magnetron Sputtering: Fundamentals, Technologies, Challenges and Applications*, in edited by D. Lundin, T. Minea, and J. T. Gudmundsson (Elsevier, Amsterdam, 2020).  
<sup>24</sup>M. Samuelsson, D. Lundin, J. Jensen, M. A. Raadu, J. T. Gudmundsson, and U. Helmersson, *Surf. Coat. Technol.* **205**, 591 (2010).

22 May 2024 13:21:17

- <sup>25</sup>M. Lattemann, A. P. Ehiasarian, J. Bohlmark, P. Å. O. Persson, and U. Helmersson, *Surf. Coat. Technol.* **200**, 6495 (2006).
- <sup>26</sup>M. Kateb, H. Hajihoseini, J. T. Gudmundsson, and S. Ingvarsson, *J. Vac. Sci. Technol. A* **37**, 031306 (2019).
- <sup>27</sup>D. Xie, L. J. Wei, H. Y. Liu, K. Zhang, Y. X. Leng, D. T. A. Matthews, and R. Ganesan, *Surf. Coat. Technol.* **442**, 128192 (2022).
- <sup>28</sup>J. Alami, P. O. Å. Petersson, D. Music, J. T. Gudmundsson, J. Bohlmark, and U. Helmersson, *J. Vac. Sci. Technol. A* **23**, 278 (2005).
- <sup>29</sup>M. N. Polyakov, *et al.*, *Surf. Coat. Technol.* **368**, 88 (2019).
- <sup>30</sup>A. Butler, N. Brenning, M. A. Raadu, J. T. Gudmundsson, T. Minea, and D. Lundin, *Plasma Sources Sci. Technol.* **27**, 105005 (2018).
- <sup>31</sup>T. Kubart, M. Čada, D. Lundin, and Z. Hubička, *Surf. Coat. Technol.* **238**, 152 (2014).
- <sup>32</sup>D. Lundin, M. Čada, and Z. Hubička, *Plasma Sources Sci. Technol.* **24**, 035018 (2015).
- <sup>33</sup>H. Hajihoseini, M. Čada, Z. Hubička, S. Ūnaldi, M. A. Raadu, N. Brenning, J. T. Gudmundsson, and D. Lundin, *Plasma* **2**, 201 (2019).
- <sup>34</sup>M. Rudolph, N. Brenning, H. Hajihoseini, M. A. Raadu, J. Fischer, J. T. Gudmundsson, and D. Lundin, *J. Vac. Sci. Technol. A* **40**, 043005 (2022).
- <sup>35</sup>N. Brenning, A. Butler, H. Hajihoseini, M. Rudolph, M. A. Raadu, J. T. Gudmundsson, T. Minea, and D. Lundin, *J. Vac. Sci. Technol. A* **38**, 033008 (2020).
- <sup>36</sup>H. Hajihoseini, M. Čada, Z. Hubička, S. Ūnaldi, M. A. Raadu, N. Brenning, J. T. Gudmundsson, and D. Lundin, *J. Vac. Sci. Technol. A* **38**, 033009 (2020).
- <sup>37</sup>R. Franz, C. Clavero, J. Kolbeck, and A. Anders, *Plasma Sources Sci. Technol.* **25**, 015022 (2016).
- <sup>38</sup>N. Britun, M. Palmucci, S. Konstantinidis, and R. Snyders, *J. Appl. Phys.* **117**, 163302 (2015).
- <sup>39</sup>N. Britun, M. Palmucci, S. Konstantinidis, and R. Snyders, *J. Appl. Phys.* **117**, 163303 (2015).
- <sup>40</sup>J. Hnilica, P. Klein, P. Vašina, R. Snyders, and N. Britun, *J. Appl. Phys.* **128**, 043303 (2020).
- <sup>41</sup>J. Hnilica, P. Klein, P. Vašina, R. Snyders, and N. Britun, *J. Appl. Phys.* **128**, 043304 (2020).
- <sup>42</sup>A. D. Pajdarová, T. Kozák, J. Čapek, and T. Tölg, *Plasma Sources Sci. Technol.* **31**, 05LT04 (2022).
- <sup>43</sup>D. J. Christie, *J. Vac. Sci. Technol. A* **23**, 330 (2005).
- <sup>44</sup>A. Anders, J. Andersson, and A. Ehiasarian, *J. Appl. Phys.* **102**, 113303 (2007).
- <sup>45</sup>D. Lundin, N. Brenning, D. Jadernas, P. Larsson, E. Wallin, M. Lattemann, M. A. Raadu, and U. Helmersson, *Plasma Sources Sci. Technol.* **18**, 045008 (2009).
- <sup>46</sup>T. Shimizu, M. Zanaška, R. P. Villoan, N. Brenning, U. Helmersson, and D. Lundin, *Plasma Sources Sci. Technol.* **30**, 045006 (2021).
- <sup>47</sup>G. Greczynski and L. Hultman, *Vacuum* **124**, 1 (2016).
- <sup>48</sup>M. Rudolph, N. Brenning, H. Hajihoseini, M. A. Raadu, T. M. Minea, A. Anders, D. Lundin, and J. T. Gudmundsson, *J. Phys. D: Appl. Phys.* **55**, 015202 (2022).
- <sup>49</sup>N. Brenning, H. Hajihoseini, M. Rudolph, M. A. Raadu, J. T. Gudmundsson, T. M. Minea, and D. Lundin, *Plasma Sources Sci. Technol.* **30**, 015015 (2021).
- <sup>50</sup>D. Lundin, C. Vitelaru, L. de Poucques, N. Brenning, and T. Minea, *J. Phys. D: Appl. Phys.* **46**, 175201 (2013).
- <sup>51</sup>P. Atkins and J. de Paula, *Atkins' Physical Chemistry*, 10th ed. (Oxford University Press, Oxford, 2014), Table 21.1.
- <sup>52</sup>S. Kunze, R. Groll, B. Besser, and J. Thöming, *Sci. Rep.* **12**, 2057 (2022).
- <sup>53</sup>J. Balakrishnan, I. D. Boyd, and D. G. Braun, *J. Vac. Sci. Technol. A* **18**, 907 (2000).
- <sup>54</sup>M. Rudolph, N. Brenning, M. A. Raadu, H. Hajihoseini, J. T. Gudmundsson, A. Anders, and D. Lundin, *Plasma Sources Sci. Technol.* **29**, 05LT01 (2020).
- <sup>55</sup>C. Huo, D. Lundin, J. T. Gudmundsson, M. A. Raadu, J. W. Bradley, and N. Brenning, *J. Phys. D: Appl. Phys.* **50**, 354003 (2017).
- <sup>56</sup>J. Vlček and K. Burcalová, *Plasma Sources Sci. Technol.* **19**, 065010 (2010).
- <sup>57</sup>M. Rudolph, H. Hajihoseini, M. A. Raadu, J. T. Gudmundsson, N. Brenning, T. M. Minea, A. Anders, and D. Lundin, *J. Appl. Phys.* **129**, 033303 (2021).
- <sup>58</sup>H. Hajihoseini, N. Brenning, M. Rudolph, M. A. Raadu, D. Lundin, J. Fischer, T. M. Minea, and J. T. Gudmundsson, *J. Vac. Sci. Technol. A* **41**, 013002 (2023).